

# Neural circuits in the mouse retina support color vision in the upper visual field

Klaudia P. Szatko<sup>1-3\*</sup>, Maria M. Korympidou<sup>1,3,4\*</sup>, Yanli Ran<sup>1,4</sup>, Philipp Berens<sup>1,2,5</sup>, Deniz Dalkara<sup>6</sup>, Timm Schubert<sup>1,4</sup>, Thomas Euler<sup>1,2,4</sup>, Katrin Franke<sup>1,2,#</sup>

<sup>1</sup>Institute for Ophthalmic Research, University of Tübingen, Germany

<sup>2</sup>Bernstein Center for Computational Neuroscience, University of Tübingen, Germany

<sup>3</sup>Graduate Training Center of Neuroscience, International Max Planck Research School, University of Tübingen, Germany

<sup>4</sup>Center for Integrative Neuroscience, University of Tübingen, Germany

<sup>5</sup>Institute for Bioinformatics and Medical Informatics, University of Tübingen, Germany

<sup>6</sup>Sorbonne Université, INSERM, CNRS, Institut de la Vision, Paris, France

\*These authors contributed equally to this work

#Correspondence at [katrin.franke@cin.uni-tuebingen.de](mailto:katrin.franke@cin.uni-tuebingen.de)

## ABSTRACT

Color vision is essential to the survival of most animals. Its neural basis lies in the retina, where chromatic signals from different photoreceptor types sensitive to distinct wavelengths are locally compared by neural circuits. Mice, like most mammals, are generally dichromatic and have two cone photoreceptor types. However, in the ventral retina most cones display the same spectral preference, impairing spectral comparisons necessary for color vision. This conflicts with behavioral evidence showing that mice can discriminate colors only in the corresponding upper visual field. Here, we systematically investigated the neural circuits underlying mouse color vision across three processing stages of the retina by recording the output of cones, bipolar and ganglion cells using two-photon imaging. Surprisingly, we found that across all retinal layers most color-opponent cells were located in the ventral retina. This started at the level of the cone output, where color-opponency was mediated by horizontal cells and likely involving rod photoreceptors. Next, bipolar cells relayed the chromatic information to ganglion cells in the inner retina, where type-specific, non-linear center-surround interactions resulted in specific color-opponent output channels to the brain. This suggests that neural circuits in the mouse retina are specifically tuned to extract color information from the upper visual field, aiding robust detection of aerial predators and ensuring the animal's survival.

## 37 INTRODUCTION

38 Color vision is key to guiding behavior in animals (reviewed in (Gerl and Morris, 2008)),  
39 including navigating in ecological niches (e.g. (Pfeiffer and Homberg, 2007)), communicating  
40 with conspecifics (e.g. (Huang et al., 2014)), foraging as well as detecting predators and prey  
41 (e.g. (Dominy and Lucas, 2001; Potier et al., 2018)). In the retina, signals from different  
42 photoreceptor types sensitive to different wavelengths are locally compared by downstream  
43 retinal circuits to extract chromatic information present in the visual input (reviewed in  
44 (Thoreson and Dacey, 2019)). These circuits have been studied in detail in trichromatic  
45 primates (reviewed in (Dacey, 2000; Neitz and Neitz, 2011; Thoreson and Dacey, 2019)).  
46 Here, signals from short (S; “blue”), medium (M; “green”) and long (L; “red”)  
47 wavelength-sensitive cone photoreceptors are processed via two main opponent pathways:  
48 red-green (L vs. M) and blue-yellow opponency (S vs. L+M). While the former is mainly  
49 based on random and cone type-unselective wiring of the high-acuity midget system (Martin  
50 et al., 2001; Buzás et al., 2006; Field et al., 2010; Crook et al., 2011; Wool et al., 2019),  
51 blue-yellow opponency relies on precise connectivity in cone type-selective retinal circuits  
52 (Dacey and Lee, 1994; Calkins et al., 1998; Crook et al., 2009a).

53 Compared to primates, the retinal circuits underlying dichromatic vision in other mammals are  
54 far from being understood (reviewed in (Puller and Haverkamp, 2011; Marshak and Mills,  
55 2014)). This is also true for the mouse – despite its prominent role as one of today’s most  
56 frequently used model in visual neuroscience. Mice express S- and M-opsin (Szél et al.,  
57 1992) most sensitive to UV and green light, respectively (Fig. 1a) (Jacobs et al., 1991; Baden  
58 et al., 2013). In addition, M-cones co-express S-opsin, with co-expression increasing towards  
59 the ventral retina (Fig. 1b) (Röhlich et al., 1994; Applebury et al., 2000). In contrast, S-cones  
60 exclusively expressing S-opsin (“true” S-cones) make up ~5% of all cones and are  
61 homogeneously distributed across the retina (Haverkamp et al., 2005). This asymmetric  
62 opsin distribution results in a mainly green-sensitive dorsal and a UV-sensitive ventral retina  
63 (Calderone and Jacobs, 1995; Baden et al., 2013). Nonetheless, behavioral studies have  
64 demonstrated that mice can discriminate between light spots of different colors (Jacobs et al.,  
65 2004), at least in the upper visual field (Denman et al., 2018). However, the retinal circuits  
66 underlying this behavior are largely unknown.

67 Several neuronal circuits for S vs. M color-opponency have been previously proposed in the  
68 mouse retina. Some of these circuits involve wiring with S-cone-selective type 9 bipolar cells  
69 (BCs) (Stabio et al., 2018). Others do not require cone type-selective connectivity: For  
70 example, alpha retinal ganglion cells (RGCs) located along the horizontal midline exhibit  
71 color-opponent responses due to chromatically distinct input to their center and surround  
72 (Chang et al., 2013). In addition, rod photoreceptors, whose spectral sensitivity closely  
73 matches that of M-cones, may also be involved in color-opponency: They provide an  
74 antagonistic surround to JAM-B RGCs located in the S-opsin dominated ventral retina by  
75 lateral feedback from horizontal cells (HCs) (Joesch and Meister, 2016). Such a rod-cone  
76 opponent mechanism may support color discrimination in the ventral retina despite the lack of  
77 substantial M-opsin expression. While all these studies point at the existence of  
78 color-opponent signals downstream from mouse photoreceptors, a comprehensive survey of  
79 chromatic processing and the retinal circuits underlying mouse color vision (Jacobs et al.,  
80 2004; Denman et al., 2018) is still missing.

81 Therefore, we systematically investigated the basis for color vision in the mouse retina across  
82 three consecutive processing stages. We recorded the output signals of cones, BCs and  
83 RGCs to chromatic visual stimulation in the *ex-vivo*, whole-mounted retina using two-photon  
84 calcium and glutamate imaging. Surprisingly, we found that across all processing layers,  
85 color-opponency was largely confined to the S-opsin dominated ventral retina. Here,  
86 color-opponent responses were already present at the level of the cone output, mediated by  
87 input from HCs and likely involving rod photoreceptors. We further show how BCs forward the  
88 chromatic signals from photoreceptors to the inner retina, where different RGC types  
89 integrate information from their center and surround in a type specific way, thereby increasing  
90 the diversity of chromatic signals available to the brain.

91

## 92 RESULTS

### 93 Recording chromatic cone responses in the whole-mounted mouse retina

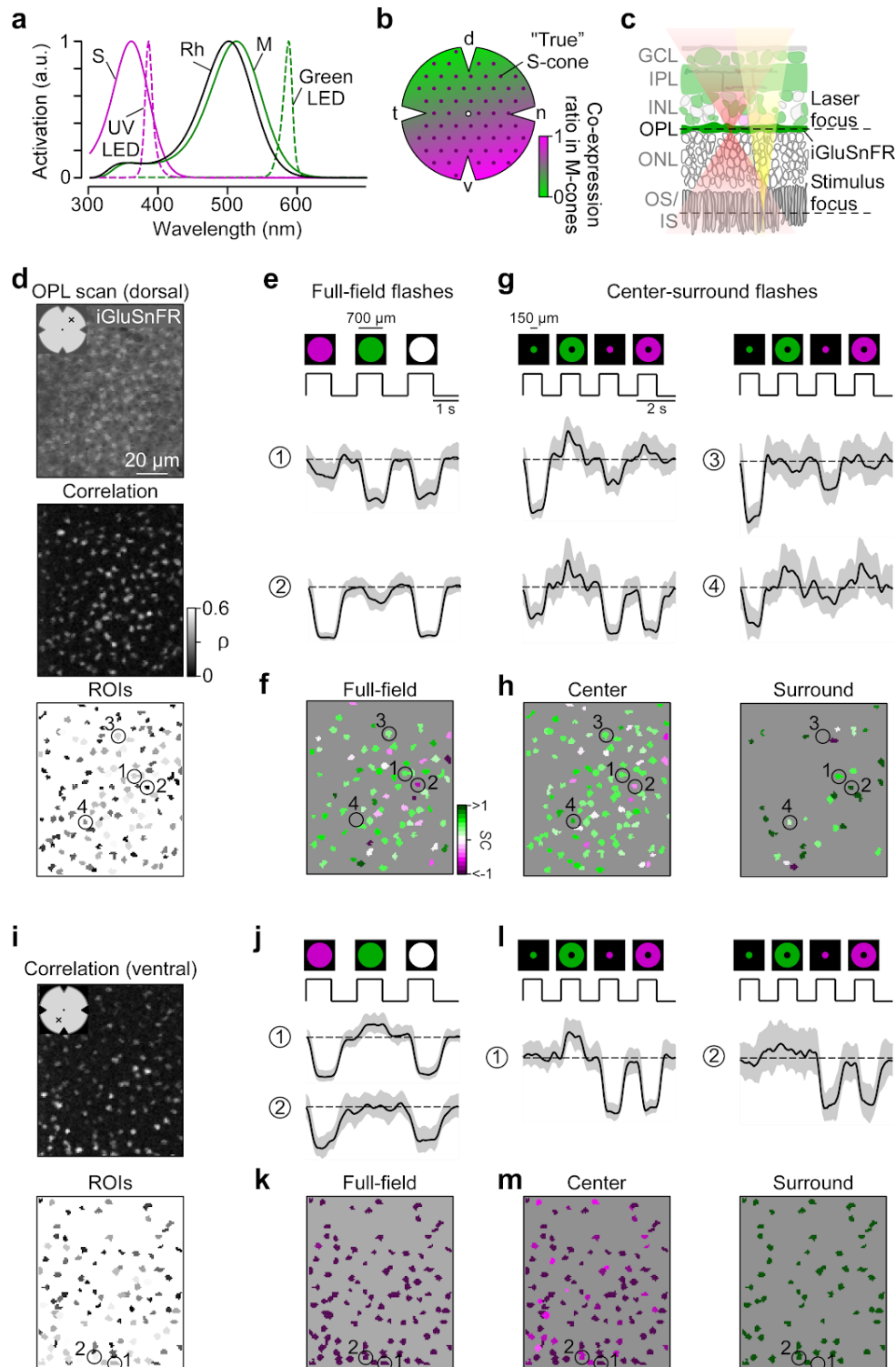
94 To characterize chromatic signaling in cones, we recorded synaptic glutamate release from  
95 their axon terminals. To this end, we expressed the glutamate biosensor iGluSnFR (Marvin et  
96 al., 2013) ubiquitously in the retina using a viral approach (Fig. 1c) (Franke et al., 2017). In  
97 the outer plexiform layer (OPL), where the cone axon terminals are located, this approach  
98 resulted in iGluSnFR being predominantly expressed in HC processes (Chapot et al., 2017),  
99 which are postsynaptic to the photoreceptors. To identify functional release units, we defined  
100 regions of interest (ROIs) using a correlation-based approach (Fig. 1d,i; Methods). These  
101 functionally defined ROIs formed a regular mosaic within individual scan fields (Suppl. Fig.  
102 S1a-h), reminiscent to the mosaic of EM-reconstructed cone axon terminals (Wässle and  
103 Riemann, 1978; Behrens et al., 2016). In addition, the ROIs co-localized with anatomical  
104 cone axon terminals visualized using Sulforhodamine-101 (SR-101; Suppl. Fig. S1i) (Chapot  
105 et al., 2017). Together, this suggests that our ROIs correspond to individual cone axon  
106 terminals and that densely packed rod photoreceptors – the only other source of glutamate  
107 release in the outer retina – do not contribute detectably to the glutamate signals recorded in  
108 the OPL (Discussion). For simplicity, we will in the following refer to ROIs in OPL scan fields  
109 as cones.

110 In total, we recorded light-evoked glutamate responses from 2,945 cones (n=52 scan fields,  
111 n=9 mice) located in dorsal and ventral retina using full-field (700  $\mu\text{m}$  in diameter) as well as  
112 center (150  $\mu\text{m}$  in diameter) and surround (annulus; full-field – center) green and UV light  
113 flashes (Fig. 1e,g; Methods). For each cone that passed our quality criterion (Methods), we  
114 quantified the chromatic preference of full-field, center and surround responses by estimating  
115 the spectral contrast (SC; for UV- and green-sensitivity  $SC < 0$  and  $SC > 0$ , respectively). For  
116 sufficient center stimulation of all cones within one scan field, the size of the center stimulus  
117 was slightly larger than the size of the scan field and, hence, did not relate to the anatomical  
118 size of cones.

### 119 Ventral cone photoreceptors display color-opponent responses

120 We found that the chromatic preference of cone full-field and center responses largely  
121 matched the opsin expression across the mouse retina. Generally, as vertebrate cones are  
122 Off cells and hyperpolarize upon an increase in light, cone center and full-field responses  
123 were characterized by a decrease in glutamate release (Fig. 1e,g). In agreement with the  
124 predominance of M-opsin in the dorsal retina, the majority of dorsal cones displayed a strong  
125 response to green full-field and center flashes (Figs. 1e-h, 2a,b;  $SC_{center} = 0.38 \pm 0.44$ ,  
126  $SC_{full-field} = 0.37 \pm 0.45$ ). Due to the long sensitivity tail of M-opsin to shorter wavelengths (cf. Fig.  
127 1a), most dorsal cones showed a small additional response to UV. In addition, consistent with  
128 the homogeneous distribution of S-cones (Haverkamp et al., 2005), a small number of dorsal  
129 cones responded strongly to UV light (see e.g. cone (2) in Fig. 1e-h). Ventral cones exhibited  
130 UV-dominant responses to full-field and center flashes (Figs. 1j-m, 2a,b;  $SC_{center} = -0.7 \pm 0.43$ ,  
131  $SC_{full-field} = -1.12 \pm 0.43$ ), as expected from the co-expression of S-opsin in ventral M-cones (e.g.  
132 (Applebury et al., 2000)).

133



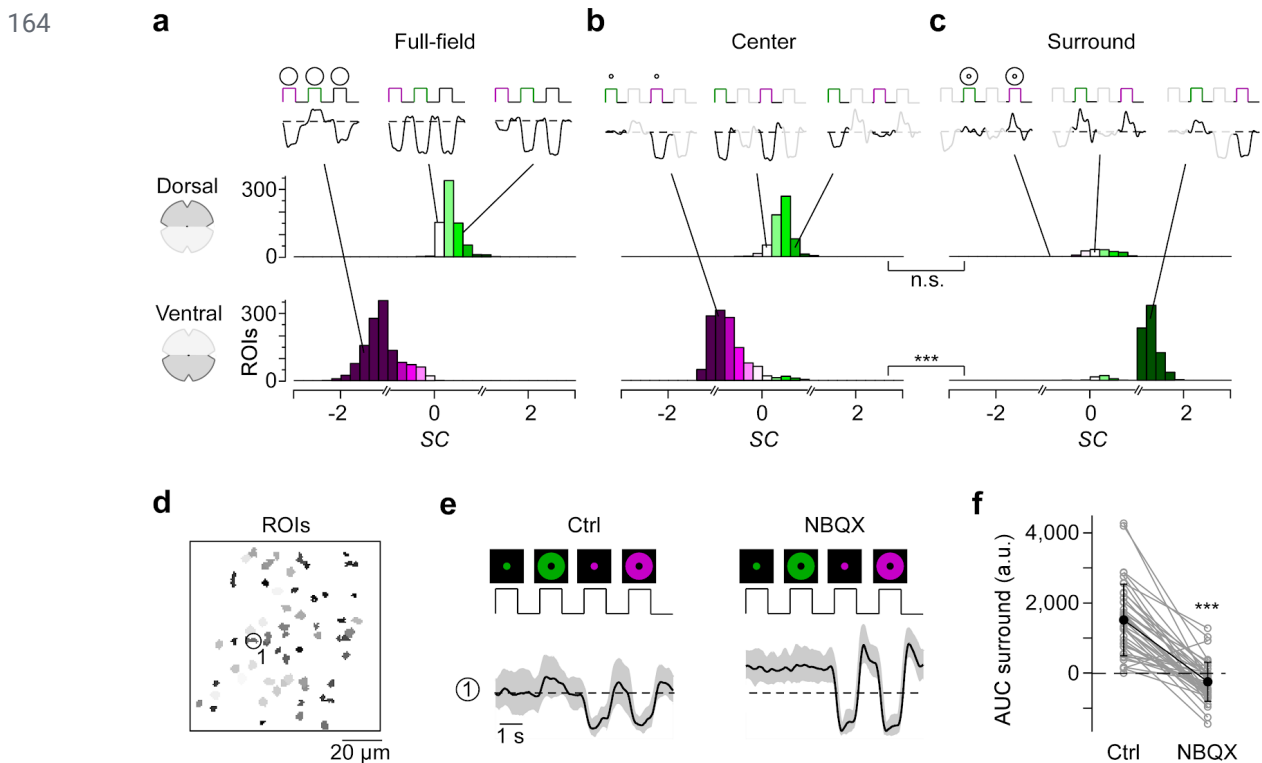
134

**Figure 1 | Imaging chromatic signals from cone axon terminals in the whole-mounted mouse retina. a,** Sensitivity spectra of mouse S- (magenta) and M-opsin (green) and rhodopsin (black; Rh), with emission spectra of UV (magenta, dotted) and green LED (green, dotted) used in the visual stimulator. **b,** Schematic illustrating the distribution of cone photoreceptors across the mouse retina. Dots and shading represent distribution of “true” S-cones and co-expression ratio of S- and M-opsin in mouse M-cones, respectively. d: dorsal; n: nasal; v: ventral; t: temporal. **c,** Schematic illustrating the experimental setup for cone recordings. OS/IS: outer/inner segment; ONL: outer nuclear layer; OPL: outer plexiform layer; INL: inner nuclear layer; IPL: inner plexiform layer; GCL: ganglion cell layer. Red and yellow shading illustrate laser and stimulus beam, respectively. **d,** Example scan field (93x110  $\mu\text{m}$ , 3.9 Hz) located in the dorsal retina, showing iGluSnFR expression in the OPL (top), correlation image (middle) and respective ROI mask (bottom). For display, the light artifact on the left side of scan fields was cut, resulting in 108x128 pixels (instead of 128x128). **e,** Cone responses of exemplary ROIs from (d, bottom) to

144

145 full-field UV, green and white flashes. As vertebrate photoreceptors are Off cells, light responses correspond to a  
 146 decrease in glutamate release. Traces show mean glutamate release with s.d. shading. Dotted line indicates  
 147 baseline. **f**, Cells from (d, bottom) color-coded according to their SC in response to full-field flashes. **g**, Glutamate  
 148 traces of cells from (d, bottom) in response to UV and green center and surround flashes. **h**, Cells from (d, bottom)  
 149 color-coded based on center (left) and surround SC (right). **i**, Correlation image (top) and ROI mask (bottom) for  
 150 an exemplary scan field located in the ventral retina. **j-m**, Like (e-h), but for cells shown in (i, bottom).

151 In contrast to full-field and center responses, the chromatic preference of cone surround  
 152 responses did not strictly follow the opsin distribution across the retina. We focused on  
 153 antagonistic responses where center and surround stimuli result in decrease and increase in  
 154 glutamate release, respectively. We found that many dorsal cones showed a stronger  
 155 increase in glutamate to green than to UV surround stimulation (Figs. 1g,h, 2c;  
 156  $SC_{surround}=0.39\pm 1.02$ ;  $n=216/671$ ), matching the spectral preference of center and full-field  
 157 responses. Most ventral cones showed an increase in glutamate solely to green surround  
 158 stimuli (Figs. 1l,m, 2c;  $SC_{surround}=1.2\pm 0.42$ ;  $n=841/1,337$ ), contrasting their UV preference for  
 159 center and full-field responses. This resulted in color-opponent center-surround RFs and  
 160 color-opponent full-field responses (Figs. 1j,k, 2a;  $SC_{full-field}<-1$ ;  $n=937/1,329$ ). Surprisingly,  
 161 UV-sensitive cones in ventral and dorsal scan fields consistently showed the same response  
 162 polarity for both UV center and surround stimulation (see e.g. cones (1) and (2) in Fig. 1l),  
 163 which might be due to increased scattering of UV light (Discussion).



165 **Figure 2 | Differential chromatic processing in ventral and dorsal cones.** **a-c**, Distribution of spectral contrast  
 166 (SC) of dorsal (top) and ventral (bottom) cones in response to full-field (a), center (b) and surround (c) flashes.  
 167 Mean glutamate traces of single cones above histograms illustrate the diversity of cone responses to chromatic  
 168 stimuli. Interestingly, only a fraction of cones showed antagonistic surround responses characterized by an  
 169 increase in glutamate release (Discussion). Breaks in the x axis indicate where different equations for estimating  
 170 SC were used (Methods). n.s.: not significant ( $p>0.05$ ); \*\*\*:  $p<0.001$ ; linear mixed-effects model for partially paired  
 171 data (for details, see Methods and Suppl. Information). **d**, ROI mask of scan field located in ventral retina. **e**,  
 172 Glutamate traces of exemplary cone from (d) in response to UV and green center and surround flashes under  
 173 control and drug condition (50  $\mu$ M NBQX). Traces show mean glutamate release with s.d. shading. **f**, Effect of

174 bath-applied NBQX on area under the curve (AUC) of green-sensitive surround responses of ventral cones (n=40  
175 ROIs, n=3 scan fields, n=2 mice). \*\*\*:  $p < 0.001$ ; Wilcoxon signed-rank test.

176 Next, we investigated the origin of the green surround responses in the ventral retina. As  
177 S-opsin expression strongly increases towards the ventral retina, the main source of green  
178 sensitivity should be rod photoreceptors (*cf.* Fig. 1a). Recently, it has been proposed that rod  
179 signals are relayed to cones via HCs (Joesch and Meister, 2016). To test this hypothesis, we  
180 recorded cone responses to chromatic center-surround stimuli while blocking light-evoked  
181 HC feedback using NBQX, an antagonist of AMPA/kainate-type glutamate receptors (Fig.  
182 2d,e; see e.g. (Chapot et al., 2017)). This caused a significant decrease in green-sensitive  
183 surround responses in ventral cones (Fig. 2f), confirming that HCs contribute to generating  
184 color-opponent responses in cones.

185 In summary, we found that the chromatic preference of a cone's center and full-field response  
186 mirrored the overall opsin distribution at the recording site, with largely UV- and  
187 green-sensitive responses in the ventral and dorsal retina, respectively. However, while in  
188 dorsal cones the chromatic preference of center and surround was very similar, ventral cones  
189 systematically exhibited a strong green-shift in the chromatic preference of their antagonistic  
190 surround, likely involving HC input driven by rods. This results in color-opponent responses in  
191 most ventral cones, demonstrating that color-opponency is already present at the first  
192 synapse of the mouse visual system.

### 193 **Bipolar cells relay color-opponent responses of cones to the inner retina**

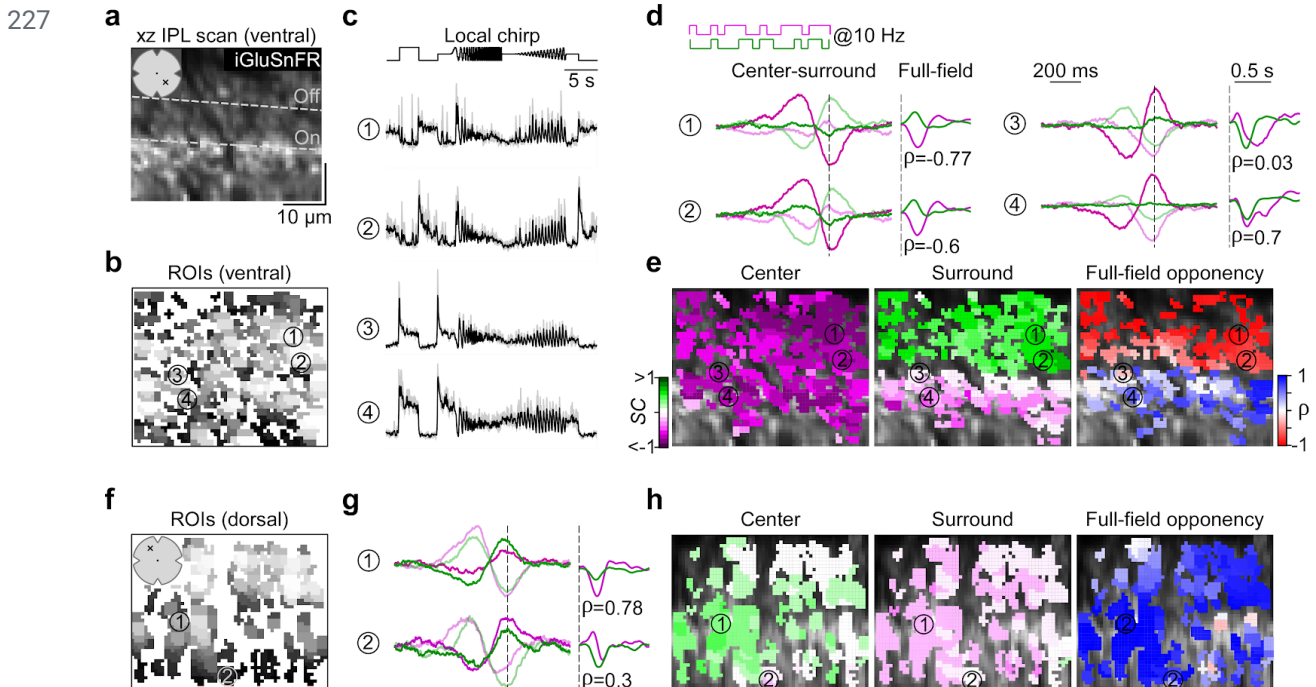
194 Next, we investigated how the chromatic information present in the cone output is relayed to  
195 the inner retina by the BC population. In the mouse retina, the signals from photoreceptors  
196 are distributed among 14 BC types (Behrens et al., 2016; Shekhar et al., 2016; Franke et al.,  
197 2017), with their axonal arbors stratifying at different levels of the inner plexiform layer (IPL)  
198 (Helmstaedter et al., 2013; Kim et al., 2014; Greene et al., 2016).

199 To record responses from BCs, we again used ubiquitous expression of iGluSnFR. In  
200 contrast to previous work (Franke et al., 2017), where the scan fields were parallel to the  
201 retinal layers, we here employed axial scanning using an electrically tunable lens to rapidly  
202 shift the focal plane of the excitation laser (Zhao et al., 2019). This allowed us to  
203 simultaneously record the glutamatergic signals across the entire IPL (Fig. 3a). Like before,  
204 we defined ROIs based on local image correlation (Fig. 3b; Methods) (Zhao et al., 2019). To  
205 register the IPL depth of each ROI, we used the two characteristic dendritic plexi of  
206 cholinergic starburst amacrine cells as landmarks (*cf.* Fig. 1b in (Franke et al., 2017)); these  
207 "ChAT bands" were visible through their TdTomato-expression in our transgenic animals.

208 In total, we recorded light-evoked BC glutamate release from 3,604 ROIs (n=21 scan fields,  
209 n=5 mice) across the entire IPL (Suppl. Fig. S2a). As expected from the type-specific axonal  
210 stratification profiles of BCs (Helmstaedter et al., 2013; Kim et al., 2014; Greene et al., 2016),  
211 ROIs located at different IPL depths showed distinct responses to the local chirp stimulus  
212 (Fig. 3c; 100  $\mu\text{m}$  in diameter). To investigate chromatic signaling in BCs, we used a 10 Hz  
213 center-surround UV and green flicker stimulus (Fig. 3d; Methods). From the glutamate  
214 responses of each ROI, we estimated the preferred stimulus ("event-triggered stimulus  
215 kernels") for the four conditions – center and surround for both UV and green – to obtain the  
216 BC ROI's chromatic RF preferences (as SC, see above). In addition, we computed the mean  
217 glutamate event of each ROI to a full-field UV and green light spot ("stimulus-triggered event

218 kernels”) to test for full-field color-opponency (quantified by the linear correlation coefficient  
 219 ( $\rho$ ) between UV and green event kernels; Methods).

220 In line with the chromatic preference of cone center responses (*cf.* Fig. 2), we found that BCs  
 221 located in the ventral and dorsal retina showed a UV- and green-dominant center,  
 222 respectively (Figs. 3d-h, 4a,b; ventral:  $SC_{center} = -0.44 \pm 0.24$ , dorsal:  $SC_{center} = 0.1 \pm 0.22$ ). Overall,  
 223 we did not observe large differences in SC of BC center responses across the IPL (Suppl.  
 224 Fig. S2b). This is consistent with recent connectomic data demonstrating that, except for type  
 225 9 and type 1 BC (Discussion), mouse BCs indiscriminately contact all cone types within their  
 226 dendritic tree (Behrens et al., 2016).



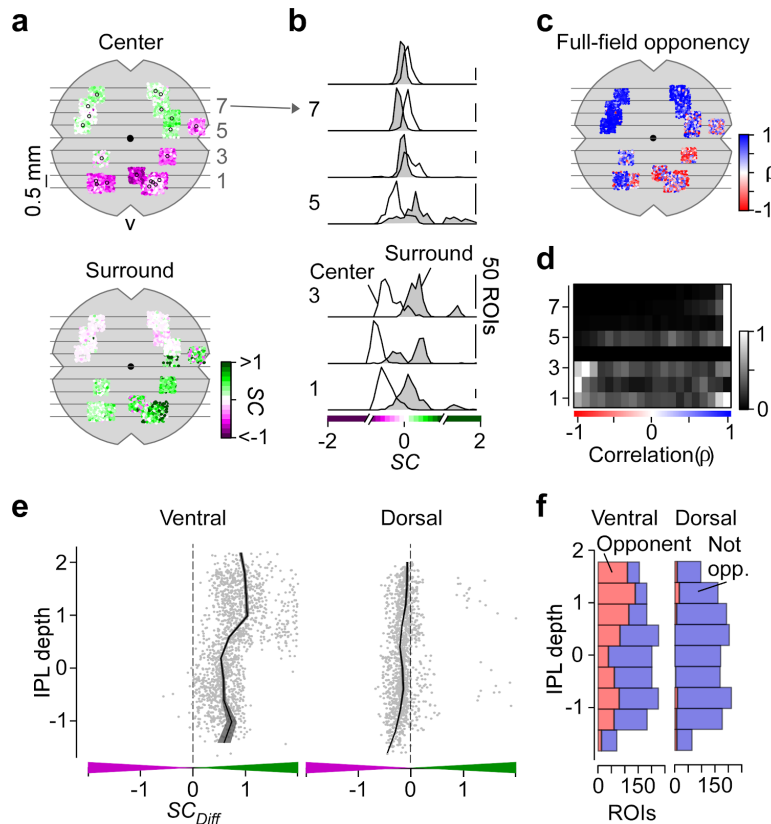
228 **Figure 3 | Recording chromatic bipolar cell responses across the inner plexiform layer.** **a**, Vertical (xz) scan  
 229 field (48x50  $\mu$ m, 11.17 Hz) located in the ventral retina showing iGluSnFR expression across the inner plexiform  
 230 layer (IPL). Dotted lines indicate On and Off ChAT band, respectively. **b**, ROI mask for scan field shown in (a). For  
 231 details on ROI detection, see Methods. **c**, Mean glutamate traces (black, s.d. shading in grey; n=5 trials) of ROIs  
 232 indicated in (b) in response to a local chirp stimulus. **d**, Temporal center (bright) and surround (dim) kernels  
 233 (event-triggered average) estimated from a 10 Hz center-surround flicker stimulus of UV and green LED (left) and  
 234 mean glutamate events (stimulus-triggered event) in response to a full-field UV and green stimulus (right) for ROIs  
 235 indicated in (b). Linear correlation coefficient ( $\rho$ ) of mean glutamate events indicated below traces. Dotted lines  
 236 indicate time point of response/stimulus. **e**, ROI mask from (b) color-coded according to center (left) and surround  
 237 spectral contrast (SC) (middle) as well as correlation (right). **f**, ROI mask of a scan field located in the dorsal  
 238 retina. **g,h**, Like (d,e), but for dorsal scan field shown in (f).

239 The chromatic preference of BC surround responses differed from that of their respective  
 240 center responses, particularly in the ventral retina. Surround responses in ventral BCs were  
 241 systematically shifted towards green ( $SC_{surround} = 0.21 \pm 0.27$ ), resulting in color-opponent  
 242 full-field responses ( $\rho < -0.3$ ) for approx. half of all ventral BC ROIs (Figs. 3d,e, 4a-d;  
 243 n=762/1,714). Notably, the difference in SC of center and surround ( $SC_{Diff}$ ) as well as the  
 244 fraction of color-opponent responses was significantly larger for ROIs located in the IPL's Off  
 245 sublamina compared to those in the On sublamina (Figs. 4e,f, S2c; Discussion). Dorsal BCs  
 246 showed a shift towards slightly higher UV-sensitivity in their surround responses (Figs. 3g,h,  
 247 4a,b;  $SC_{surround} = 0.03 \pm 0.19$ ), which was stronger for On compared to Off BCs (Fig. 4e) but  
 248 much smaller than for ventral BCs; therefore only very few (n=64/1,474) dorsal BCs showed

249 color-opponent full-field responses (Fig. 4f). In addition, we obtained comparable results  
 250 when modulating green and UV sinusoidally (Suppl. Fig. S3) – a visual stimulus often used in  
 251 retinal studies on chromatic processing (e.g. (Dacey and Lee, 1994; Chang et al., 2013)).

252 In summary, our data show that BCs provide chromatically tuned excitatory drive to  
 253 downstream amacrine cell (AC) and RGC circuits. Furthermore, the difference between On  
 254 and Off BCs indicates that they might not simply relay the chromatic information from cones  
 255 to the inner retina.

256



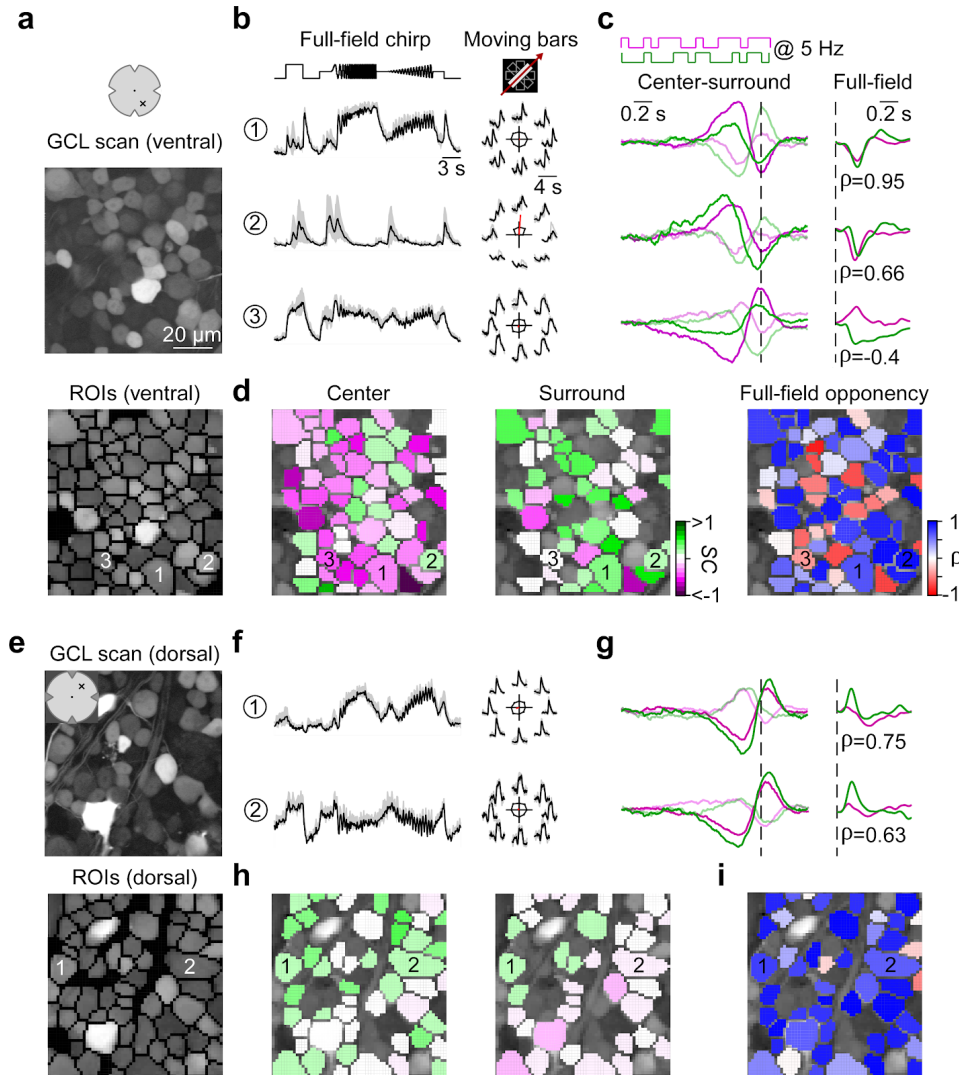
257 **Figure 4 | Chromatic signals of bipolar cells match cone responses across the retina.** **a**, Distribution of  
 258 recorded inner plexiform layer (IPL) scan fields (black circles), with ROIs color-coded according to their center  
 259 (top) and surround spectral contrast (SC; bottom). ROIs are scattered around scan field center by  $\pm 300 \mu\text{m}$  in x  
 260 and y. Grey lines and numbers on the left indicate bins used for analysis in (b) and (d). Bin size: 0.5 mm. **b**,  
 261 Distribution of center (no fill) and surround (grey fill) SC values from ventral to dorsal retina. Numbers indicate bins  
 262 shown in (a). For all bins, center SC was significantly different from surround SC (Linear mixed-effects model for  
 263 partially paired data; see Methods and Suppl. Information). **c**, Same as (a), but color-coded according to  
 264 correlation coefficient ( $\rho$ ) of full-field events. **d**, Peak-normalized histograms showing distribution of correlation  
 265 coefficients from ventral to dorsal retina. Numbers indicate bins shown in (a). Bin size: 0.5 mm. **e**, Difference of  
 266 center and surround SC ( $SC_{Diff}$ ) across the IPL for ROIs located in the ventral (left) and dorsal (right) retina.  $SC_{Diff}$   
 267 significantly varied with IPL depth for both ventral and dorsal retina (Generalized additive model; see Methods and  
 268 Suppl. Information). **f**, Distribution of full-field opponent (red;  $\rho < -0.3$ ) and non-opponent (blue) ROIs across the IPL  
 269 for ventral and dorsal scan fields. Number of opponent ROIs significantly varied with IPL depth for ventral and  
 270 dorsal retina (Generalized additive model; see Methods and Suppl. Information).

## 271 Color-opponent responses are preserved at the level of the retinal output

272 Finally, we investigated how the chromatic information is represented in the population of  
 273 RGCs. We used the synthetic calcium indicator Oregon Green BAPTA-1 (OGB-1) and  
 274 bulk-electroporation to uniformly label the ganglion cell layer (GCL; Fig. 5a) (Briggman and  
 275 Euler, 2011; Baden et al., 2016). This allowed us to densely record somatic signals from

276 RGCs and displaced ACs (dAC), which make up the mouse GCL at a ratio of roughly 1:1  
 277 (Schlamp et al., 2013). We recorded GCL scan fields at different positions along the retina's  
 278 dorso-ventral axis (*cf.* Fig. 6a). To assign the recorded cells ( $n=8,429$  cells,  $n=100$  scan  
 279 fields,  $n=20$  mice) to functional RGC and dAC groups (presumably corresponding to single  
 280 types) previously described (Baden et al., 2016), we presented two achromatic stimuli  
 281 (full-field chirp and moving bar; Fig. 5b). Like for the BC recordings, we characterized the  
 282 cells' chromatic preference and full-field opponency by estimating center-surround stimulus  
 283 and full-field event kernels, respectively, from calcium responses to a 5 Hz center-surround  
 284 UV and green flicker stimulus (center: 250  $\mu\text{m}$  in diameter) (Fig. 5c).

285



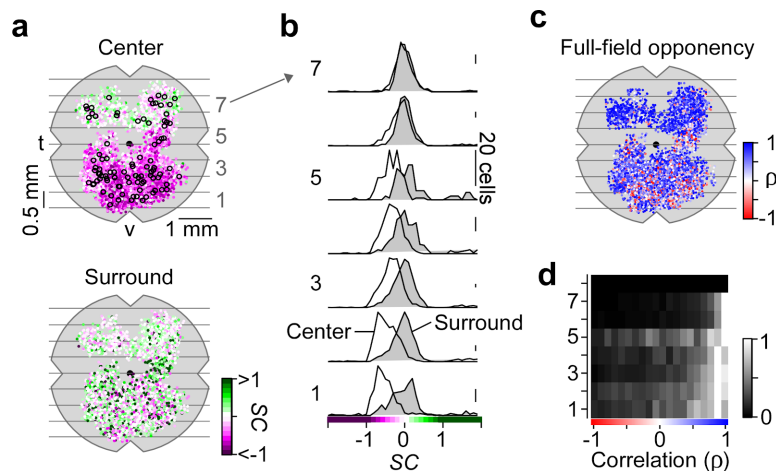
286 **Fig. 5 | Chromatic responses in the ganglion cell layer of the mouse retina.** **a**, Ganglion cell layer (GCL) scan  
 287 field (top; 95x95  $\mu\text{m}$ , 7.8125 Hz) located in the ventral retina electroporated with the synthetic calcium indicator  
 288 Oregon Green BAPTA-1 (OGB-1) and corresponding ROI mask (bottom). **b**, Mean calcium traces (black, s.d.  
 289 shading in grey;  $n=5$  trials) of ROIs indicated in (a, bottom) in response to full-field chirp (left) and moving bars  
 290 (right). **c**, Temporal center (bright) and surround (dim) kernels estimated from a 5 Hz center-surround flicker  
 291 stimulus of UV and green LED (left) and mean calcium events in response to a full-field UV and green stimulus  
 292 (right) for ROIs indicated in (a, bottom). Linear correlation coefficient of full-field events indicated below traces.  
 293 Dotted lines indicate time point of response/stimulus. **d**, ROIs from (a, bottom) color-coded according to center  
 294 (left) and surround spectral contrast (SC; middle) as well as correlation (right). **e**, Scan field and corresponding  
 295 ROI mask located in the dorsal retina. **f-i**, Like (b-d), but for scan field shown in (e).

296 We found that the chromatic preference of GCL cell center responses largely matched the  
 297 opsin expression, with a gradient of UV- to green-dominated responses from ventral to dorsal  
 298 retina (Figs. 5d,h, 6a,b; ventral:  $SC_{center} = -0.35 \pm 0.27$ , dorsal:  $SC_{center} = 0.06 \pm 0.25$ ). Notably, the  
 299 chromatic tuning of center responses was more diverse in the GCL compared to the IPL  
 300 (Suppl. Fig. S4). For example, we frequently observed ventral GCL cells responding stronger  
 301 to green than to UV center stimulation (Fig. 5c,d), which was not the case for ventral OPL  
 302 and IPL recordings.

303 Surround responses of ventral GCL cells were systematically shifted towards green (Figs.  
 304 5c,d, 6a,b;  $SC_{surround} = 0.21 \pm 0.82$ ), resulting in a large difference in center vs. surround  
 305 chromatic preference and, thus, in color-opponent full-field responses ( $n=459/3,418$ ). For  
 306 dorsal scan fields, the difference between center and surround chromatic preference and,  
 307 likewise, the fraction of color-opponent responses was smaller ( $SC_{surround} = 0.17 \pm 0.62$ ;  
 308  $n=80/1,371$ ). Interestingly, in our dataset we only rarely observed GCL cells with  
 309 center-opponent responses (Suppl. Fig. S5; Discussion), which have been found in primates  
 310 (e.g. (Crook et al., 2009b)) and some dichromatic mammals (e.g. (Sher and DeVries, 2012)).

311

312



313 **Fig. 6 | Color-opponency at the level of the mouse retinal output.** **a**, Distribution of recorded ganglion cell  
 314 layer (GCL) scan fields (black circles), with ROIs color-coded according to their center (top) and surround spectral  
 315 contrast (SC; bottom). ROIs are scattered around scan field center by  $\pm 300 \mu\text{m}$  in x and y. Grey lines and  
 316 numbers on the left indicate bins used for analysis in (b) and (d). Bin size: 0.5 mm. **b**, Distribution of center (no fill)  
 317 and surround (grey fill) SC values from ventral to dorsal retina. Numbers indicate bins shown in (a). For all bins,  
 318 center SC was significantly different from surround SC (Linear mixed-effects model for partially paired data; see  
 319 Methods and Suppl. Information). **c**, Same as (a), but color-coded according to correlation of full-field events ( $\rho$ ).  
 320 **d**, Peak-normalized histograms showing distribution of correlation coefficient from ventral to dorsal retina.  
 321 Numbers indicate bins shown in (a). Bin size: 0.5 mm.

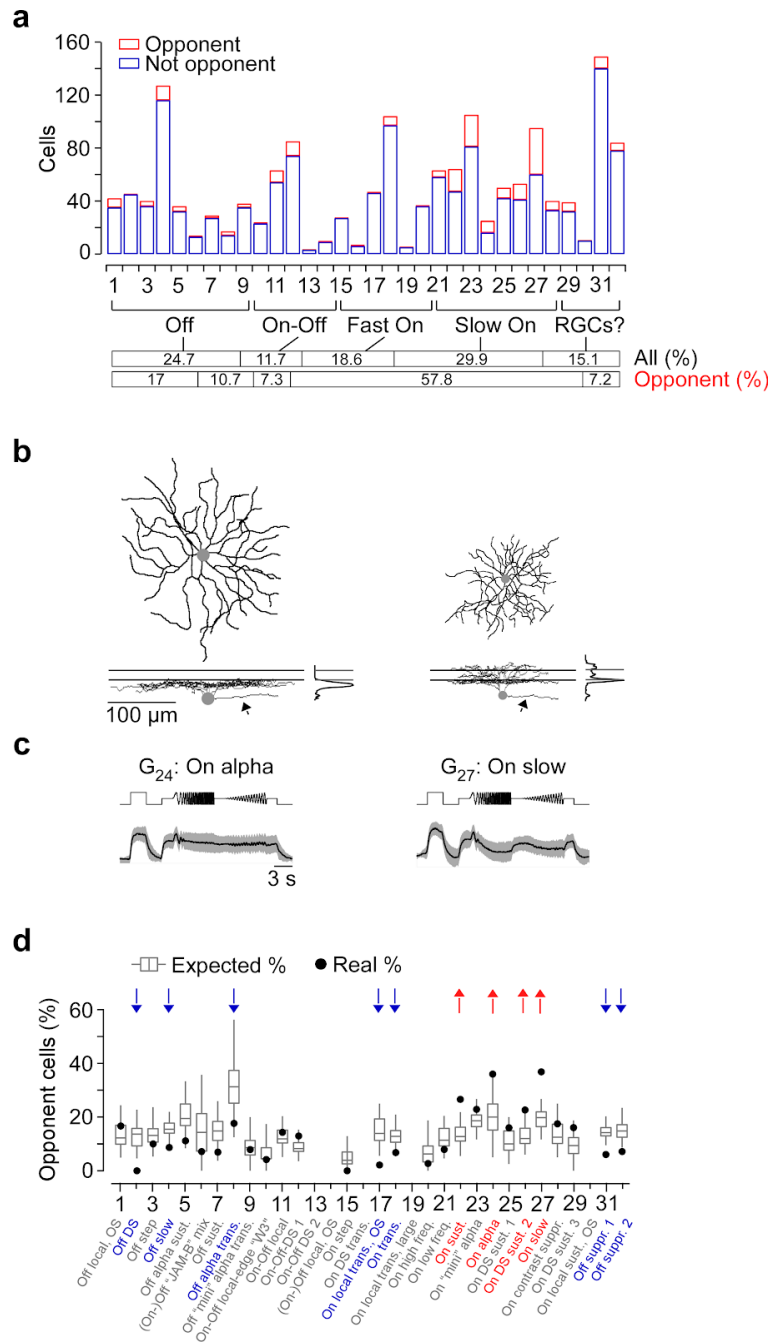
322 In summary, while color-opponency was largely preserved at the level of the retina's output  
 323 layer, our findings suggest that the complexity of chromatic signals increases from the IPL to  
 324 the GCL. Next, we investigated whether the color-opponent GCL cells correspond to RGCs  
 325 and/or dACs and if chromatic information is processed in a type-specific manner.

### 326 Cell-type specific chromatic processing in mouse retinal ganglion cells

327 We next allocated the recorded cells to the previously described functional RGC and dAC  
 328 groups (Baden et al., 2016) based on their responses to the achromatic stimuli (Methods).  
 329 Because color-opponency was pronounced in the ventral retina, we focused the analysis on  
 330 ventral scan fields. We found that color-opponent GCL cells were assigned to both RGC and

331 dAC groups (Fig. 7a, Suppl. Fig. S6), suggesting that color-opponency is a feature of both  
 332 cell classes. To verify this, we dye-injected and morphologically reconstructed color-opponent  
 333 GCL cells (n=19) subsequent to functional imaging (Fig. 7b, Suppl. Fig. S7). Consistent with  
 334 the abundance of color-opponent responses in the GCL (*cf.* Fig. 5c), we found a large variety  
 335 of dendritic morphologies in our sample, with approx. half (n=8) of the reconstructed cells  
 336 corresponding to dACs, as identified by the absence of an axon. Due to similar response  
 337 profiles, 5/19 morphologically identified RGCs and dACs were assigned to the wrong class  
 338 (Suppl. Fig. S7). Because we were interested in chromatic retinal output, in the following we  
 339 focused on RGCs (for dACs, see Suppl. Fig. S6).

340



341 **Fig. 7 | The color-opponent output channels of the mouse retina.** **a**, Distribution of ventral color-opponent  
 342 (red) and non-opponent (blue) RGCs located in the ventral retina. For analysis in (d), only groups with n>10 cells  
 343 were used. **b**, Dendritic morphologies with stratification profiles of two color-opponent cells assigned to RGC  
 344 groups G<sub>24</sub> and G<sub>27</sub>, dye-filled and reconstructed subsequent to imaging experiments. Lines for side-view of

345 morphology and stratification profile indicate On and Off ChAT bands. Arrows point at axon present only for RGCs  
346 and not for dACs. **c**, Mean full-field chirp responses (black, s.d. shading in grey;  $n=5$  trials) of RGC groups shown  
347 in (b). **d**, Box plots show distribution of expected percentages of color-opponent cells given center  $SC$  and  $SC_{Diff}$   
348 values in each group (for details, see Methods). Black circles indicate true percentage of color-opponent cells.  
349 Arrows pointing down- and up indicate groups with significantly more and less color-opponent cells than expected,  
350 respectively.

351 Ventral color-opponent RGCs were assigned to diverse functional groups, including Off,  
352 On-Off and On groups (Fig. 7a). Most RGC groups (20/32) contained at least a few ( $n \geq 3$ )  
353 color-opponent cells, indicating that color-opponency may partially be inherited from BCs (*cf.*  
354 Fig. 4). Surprisingly, the fraction of color-opponent cells greatly varied across groups: Most  
355 color-opponent RGCs were assigned to groups displaying slow On responses. For example,  
356 many sustained On alpha cells ( $G_{24}$ ) showed color-opponent responses (Fig. 7a-c),  
357 consistent with an earlier study (Chang et al., 2013). In addition, color-opponency was a  
358 prominent feature in  $G_{27}$ , which exhibited a bistratified morphology (Fig. 7b, Suppl. Fig. S7),  
359 reminiscent of RGC type 73 in (Bae et al., 2018). In contrast to BCs, where Off cells were  
360 more likely to be color-opponent than On cells, most Off as well as transient On RGC groups  
361 contained only few color-opponent cells. This difference between BCs and RGCs suggests  
362 that RGC color-opponency is not only inherited from BCs (Discussion).

363 The most parsimonious explanation for such RGC type-dependent differences in fraction of  
364 color-opponent cells is that groups differ in their center and surround spectral preference,  
365 with a larger difference between these two preferences resulting in more color-opponent  
366 cells. Additionally, non-linear integration of center and surround chromatic information could  
367 lead to pronounced color-opponency in specific RGC groups. To distinguish between these  
368 two possibilities, we tested how well the percentage of color-opponent cells within a group  
369 was explained by its chromatic preference using a permutation test: For each group with  $>10$   
370 assigned cells (27/32), we generated a distribution of expected percentages of  
371 color-opponent cells – given the cells' center and surround preference, but shuffling their  
372 group labels – and compared it to the observed percentage of color-opponent cells (Fig. 7d;  
373 Methods). We found that in approx. 60% (16/27) of all RGC groups investigated, the number  
374 of color-opponent cells was explained by the difference in chromatic preference between  
375 center and surround. However, the remaining groups showed either a significantly lower or  
376 higher percentage of color-opponent cells than expected, indicative of non-linear integration  
377 of center and surround chromatic responses in these groups. The seven groups with fewer  
378 color-opponent cells ( $G_2$ ,  $G_4$ ,  $G_8$ ,  $G_{17}$ ,  $G_{18}$ ,  $G_{31}$ ,  $G_{32}$ ) comprised a heterogeneous set of RGC  
379 groups, including Off, transient On and contrast suppressed ones (Fig. 7d). In contrast, the  
380 four groups with higher percentages of color-opponent cells than expected all showed slow  
381 On responses ( $G_{22}$ ,  $G_{24}$ ,  $G_{26}$ ,  $G_{27}$ ). Interestingly, also the three dAC groups with significantly  
382 more color-opponent cells than expected showed slow On responses (Suppl. Fig. S6), which  
383 might hint at a common circuit mechanism.

384 In summary, our data showed that color-opponency is a widespread feature among ventral  
385 RGC groups that is partially inherited by presynaptic BC circuits. However, we found  
386 evidence for non-linear integration of chromatic information in a subset of RGC groups,  
387 increasing the diversity of chromatic responses at the level of the retinal output.

388

## 389 DISCUSSION

390 Here, we systematically surveyed chromatic signaling across three consecutive processing  
391 stages in the mouse retina by population imaging of the chromatic output signals of cones,  
392 BCs and RGCs. We showed how color-opponency present in the ventral retina is already  
393 created at the cone synapse by lateral inhibition from HCs that is at least partially driven by  
394 rod photoreceptors. In addition, we demonstrated that the population of BCs then relays the  
395 chromatic information to RGCs in the inner retina, where type-specific, non-linear  
396 center-surround interactions result in specific color-opponent output channels to the brain.  
397 Our finding that color-opponency is mostly limited to the S-opsin dominant ventral retina is  
398 consistent with behavioral experiments suggesting that color vision in mice may be largely  
399 restricted to their upper visual field (Denman et al., 2018).

### 400 Chromatic processing at the first synapse of the mouse visual system

401 Many non-mammalian vertebrate species show selective wiring between distinct types of  
402 cones and HCs, which generates color-opponent responses already in the outer retina  
403 (reviewed in (Baden and Osorio, 2019; Thoreson and Dacey, 2019)). Also in the primate  
404 retina, color-opponency emerges already at the photoreceptor synapse. Here, two types of  
405 HC that preferentially contact S- or L/M-cones (Dacey et al., 1996; Chan and Grünert, 1998)  
406 provide a chromatically opponent antagonistic surround to cones (Packer et al., 2010; Crook  
407 et al., 2011). In contrast, mice and some other mammalian species only possess one HC type  
408 (Peichl and González-Soriano, 1994; Peichl et al., 1998). As it indiscriminately contacts S-  
409 and M-cones, its role in chromatic processing has been much less clear. By recording the  
410 glutamatergic output of cones in the intact, whole-mounted retina, we were able to  
411 demonstrate that also in mouse color-opponency is already present at the level of the cone  
412 output. Specifically, UV-sensitive cones located in the ventral mouse retina exhibited  
413 green-sensitive surround responses, mediated by rod-signals that are relayed to cones via  
414 HCs. This is consistent with a recent study showing that color-opponent responses of ventral  
415 JAM-B RGCs originate from a rod-cone opponent mechanism involving HCs (Joesch and  
416 Meister, 2016). The prerequisites for this rod-mediated mechanism have been experimentally  
417 established: First, mouse rods can drive visual responses at the low photopic light levels  
418 used in our experiments (Tikidji-Hamburyan et al., 2017) and, second, rod signals travel in  
419 HCs from the axon terminals to the soma via the HC axon ((Szikra et al., 2014); but see  
420 (Trümpler et al., 2008)).

421 In the following, we discuss three observations made while recording light-evoked responses  
422 from cones in the retinal whole-mount preparation.

423 First, our data suggest that the recorded glutamate signals in the OPL depict cone, but not  
424 rod signals. First, our functionally defined ROIs formed regular mosaics resembling that of  
425 the anatomical cone array (Behrens et al., 2016). Second, the ROIs co-localized with  
426 anatomically identified cone terminals. Third, we did not observe any green-sensitive  
427 hyperpolarizing responses upon center stimulation in the ventral retina, as would be expected  
428 if glutamatergic output of rod axon terminals contributed to the recorded signals. Why we did  
429 not pick up rod signals may be because of differences in the number of vesicles released  
430 (Rabl et al., 2005) and number of ribbon synapses (e.g. (Carter-Dawson and LaVail, 1979))  
431 between rods and cones. As a result, the amount of glutamate released by individual rod  
432 axon terminals may be below the detection threshold of iGluSnFR.

433 Second, a fraction of cones in our dataset did not exhibit antagonistic surround responses;  
434 this was more often the case for dorsal than ventral cones. It is unlikely that cone-to-cone  
435 differences in HC input contribute to the strong variations in surround strengths, as HCs form  
436 highly stereotypic connections with each cone's axon terminal (e.g. (Chun et al., 1996;  
437 Haverkamp et al., 2000)). Previous studies have demonstrated that the strength of HC  
438 feedback depends on functional cone properties, such as membrane potential (Verweij et al.,  
439 1996) and adaptational state (e.g. (Burkhardt, 1995)), which might vary between cells. We  
440 controlled for experimental parameters such as temperature and scan field size, while other  
441 parameters like biosensor expression and therefore laser power applied could have  
442 somewhat varied across recording fields and/or retinal locations. It is conceivable that these  
443 factors affected surround strengths in cone RFs.

444 Third, most UV-sensitive cones in both ventral and dorsal retina exhibited decreases in  
445 glutamate release to both center and surround UV stimulation. This was not the case for  
446 green-sensitive cones, which showed an increase in glutamate release when presenting a  
447 UV surround annulus. The effect observed in UV-cones could be explained by lateral signal  
448 spread due to specific cone-cone coupling (DeVries et al., 2002; Feigenspan et al., 2004)  
449 between UV-cones. Such differential coupling between different cone types has been  
450 identified in the primate retina (Hornstein et al., 2004); however, evidence for a similar  
451 mechanism in the mouse retina is missing. Alternatively, the sign-conserving surround  
452 response of UV-cones might be related to the higher sensitivity of S- compared to M-opsin  
453 expressing cones (Baden et al., 2013). Specifically, the intensity of light arising from the  
454 surround stimulus scattered within the retina may suffice to drive S-opsin but not M-opsin  
455 expressing cones.

## 456 **Mechanisms generating color-opponency in the mouse retina**

457 Depending on the mechanism used, retinal circuits extracting chromatic information can be  
458 roughly classified into two categories. "Cone type-selective pathways" rely on selective wiring  
459 of spectrally different cone types to their postsynaptic partners. In contrast, in "cone  
460 type-unselective" circuits, color-opponency generally arises as a "side-effect" of other  
461 mechanisms, such as center-surround RFs. In the following, we will summarize the evidence  
462 for each mechanism in the mouse retina and relate them to our results.

### 463 *Cone type-selective mechanisms*

464 Usually, cone type-selective retinal circuits depend on BC types that preferentially sample  
465 from specific spectral cone types. The best described example for such a cone type-selective  
466 pathway is likely the circuit generating blue-yellow opponency in the primate retina. Here, the  
467 so-called small bistratified RGC receives blue-On and yellow-Off input from BCs that  
468 exclusively contact and largely avoid S-cones, respectively (Dacey and Lee, 1994; Crook et  
469 al., 2009b). Cone type-selective BCs have also been identified in most dichromatic mammals  
470 (reviewed in (Puller and Haverkamp, 2011)). For example, mice possess an On BC type  
471 exclusively contacting S-cones (type 9) and an Off BC type that prefers M-cones (type 1)  
472 (Haverkamp et al., 2005; Breuninger et al., 2011; Behrens et al., 2016). Therefore, in dorsal  
473 scan fields we expected to find UV-dominant center responses in the innermost IPL layer,  
474 where S-cone selective type 9 BCs stratify (Haverkamp et al., 2005; Behrens et al., 2016).  
475 However, we found such responses only rarely. The low frequency of presumed type 9 BC  
476 responses resonates well with their very sparse axonal arbors. Based on EM data we  
477 estimated to find ~1 ribbon synapse per IPL scan field (*cf.* Fig. 4f in (Zhao et al., 2019)). In

478 addition, we did not observe a bias for purely green center responses in the Off sublamina of  
479 dorsal scan fields, as would be expected for M-cone preferring type 1 BCs (Breuninger et al.,  
480 2011; Behrens et al., 2016). This may be explained by a relatively small difference in  
481 chromatic preference of type 1 compared to other BC types (*cf.* Fig. 6 in (Breuninger et al.,  
482 2011)).

483 In primates, cone type-selective BCs provide separate chromatic input channels to RGCs,  
484 generating a center-opponent RF structure (Dacey and Lee, 1994; Crook et al., 2009b). In  
485 dichromatic mammals, a similar mechanism results in center-opponent RGCs in ground  
486 squirrel (Sher and DeVries, 2012) and likely guinea pig (Yin et al., 2009) and rabbit (Mills et  
487 al., 2014). Such a circuit could also exist in mice – at least in the dorsal retina where opsin  
488 co-expression is low. However, center-opponent RGC RFs were rare in our dataset and did  
489 not comprise a single functional type. For identifying center opponency, the stimulus should  
490 ideally be aligned to the RF center of the recorded cell. However, this is not possible in our  
491 population approach, where the stimulus is aligned to the center of each recording field  
492 (Methods), resulting in a spatial offset of up to 50  $\mu\text{m}$  between stimulus and RF center of the  
493 recorded cell. Therefore, we might have underestimated the number of center-opponent  
494 RGCs. Until now, there is evidence for only one mouse RGC type that uses cone  
495 type-selective BC input: It features a UV-dominant center and a green surround, with the  
496 former generated by a bias for connecting to type 9 BCs (Stabio et al., 2018). Therefore,  
497 connectivity matrices (e.g. (Helmstaedter et al., 2013; Kim et al., 2014; Behrens et al., 2016))  
498 obtained from large-scale EM reconstructions may result in further candidate cone  
499 type-selective pathways.

#### 500 *Cone type-unselective mechanisms*

501 Red-green opponency in the primate retina does not rely on cone type-selective BCs.  
502 Instead, it is a consequence of midget RGCs receiving input from one or very few M- and  
503 L-cones, resulting in either green- or red-dominant center RFs, that are compared to a yellow  
504 (M+L) surround (Martin et al., 2001; Buzás et al., 2006; Field et al., 2010; Crook et al., 2011).  
505 Similarly, two color-opponent pathways independent of cone type-selective connectivity have  
506 been identified in the mouse retina. First, the asymmetric opsin distribution can result in  
507 color-opponent responses of RGCs located along the horizontal midline due to chromatically  
508 distinct input to their center and surround (Chang et al., 2013). Second, a rod-cone opponent  
509 pathway has been linked to color-opponency in JAM-B RGCs located in the S-opsin  
510 dominated ventral retina (Joesch and Meister, 2016). Our results suggest that the latter  
511 mechanism is not restricted to a single RGC type, but that most color-opponent responses in  
512 the mouse retina are inherited from the outer retina, making color-opponency a widespread  
513 feature of ventral neurons.

514 In line with this, we found that the complete population of ventral BCs conveyed chromatic  
515 information to downstream circuits. Interestingly, the difference in center and surround  
516 chromatic preference and, therefore, the number of color-opponent responses was larger for  
517 Off compared to On BCs. The BCs' inhibitory surround could originate from HCs and/or  
518 GABAergic wide-field ACs in the outer and inner retina, respectively. We found that in the  
519 ventral retina the surround mediated by HCs is largely green-sensitive. In contrast, the  
520 surround mediated by ACs is likely UV-sensitive, as wide-field ACs receive their excitatory  
521 drive from BC center responses (e.g. (Olveczky et al., 2003; Murphy-Baum and Taylor,  
522 2015)), which, in the ventral retina, are UV-dominant. Therefore, the more pronounced  
523 color-opponency in Off BCs may be due to a stronger contribution of HCs compared to ACs

524 in generating the Off BCs' inhibitory surround. Surprisingly, this difference between On and  
525 Off BCs was not preserved at the level of the retinal output. Here, many Off RGC groups  
526 contained fewer color-opponent cells than expected from their center and surround chromatic  
527 preference. In contrast, color-opponency was significantly enriched in some slow On RGC  
528 and dAC groups. This indicates that center and surround component of RGC RFs might be  
529 driven by different BC circuits. For example, a color-opponent slow On RGC may receive  
530 center excitation from non-opponent On BCs and surround inhibition from sign-inverting ACs  
531 driven by opponent Off BCs. However, as the size of the center stimulus used for IPL and  
532 GCL recordings was different, explaining exactly how observed RGC responses arise from  
533 recorded BC responses requires further investigation.

534 In summary, our data provide little evidence for cone type-selective circuits in the mouse  
535 retina. Instead, most color-opponent responses originate in the outer retina, likely generated  
536 by a rod-cone opponent pathway. In the inner retina, chromatic information from cones is  
537 further processed, resulting in type-specific chromatic responses at the level of the retinal  
538 output.

### 539 **Functional relevance of color-opponency in mice**

540 The asymmetric opsin distribution divides the mouse retina into distinct regions. The dorsal  
541 part resembles the cone mosaic of other dichromatic mammals, with many M-cones and few  
542 S-cones (Ahnelt et al., 2006). Therefore, one would expect that the evolutionary conserved  
543 circuits that extract blue-green opponency (reviewed in (Thoreson and Dacey, 2019)) also  
544 exist in the dorsal retina of mice. In contrast, the ventral part of the mouse retina, with its  
545 M-cones co-expressing S-opsin (Röhlich et al., 1994; Applebury et al., 2000), was long  
546 considered unfit for color vision. Instead, it was linked to optimal sampling of achromatic  
547 contrast information in the sky portion of natural scenes (Baden et al., 2013). We here show  
548 that in fact, color-opponent neurons are predominantly located in the ventral retina of mice.  
549 This is in agreement with previous RGC studies (Chang et al., 2013; Joesch and Meister,  
550 2016) as well as with a recent behavioral study, which demonstrated that mice perform much  
551 better in discriminating colored light spots presented in their upper visual field (Denman et al.,  
552 2018). Using a rod-cone based mechanism to extract chromatic information in the ventral  
553 retina may be actually advantageous, because it allows color vision (Denman et al., 2018)  
554 and detecting dark objects such as predatory birds (Baden et al., 2013) through the  
555 widespread expression of S-opsin. This arrangement might also be relevant in other species  
556 with a regional increase in S-opsin density in their retina (reviewed in (Peichl, 2005)),  
557 including the common shrew (Peichl et al., 2000) or some hyenas (Calderone et al., 2003).  
558 Because mouse rod photoreceptors are active in the photopic regime (Tikidji-Hamburyan et  
559 al., 2017), rod-cone opponency likely contributes to the animal's color vision across a  
560 substantial intensity range, increasing its relevance for informing behavior.

561 According to the efficient coding theory, sensory systems adapt to the distribution of signals  
562 present in their natural environment (Barlow and BH, 1961). That color-opponency of mice  
563 appears to be largely restricted to their ventral retina suggests that behaviorally relevant  
564 chromatic information should be found in their upper visual field. It has been speculated that  
565 mice use color vision for social communication by detecting urine tags (Joesch and Meister,  
566 2016). However, urine tags large enough to appear in the upper visual field have so far only  
567 been observed for mice housed under unnatural conditions (Welch, 1953). In addition, urine  
568 might not constitute a reliable visual cue under natural conditions (Lind et al., 2013),  
569 especially since mice olfaction would be the more obvious choice to detect and analyse urine

570 cues. Alternatively, as most predators are expected to approach the mouse from above, color  
571 vision in the upper visual field could well support threat detection. Especially for visual scenes  
572 with inhomogeneous illumination (e.g. forrest), that result in large intensity fluctuations at the  
573 photoreceptor array, color-opponent RF structures may result in a more reliable signal  
574 (discussed in (Maximov, 2000; Kelber et al., 2003)).

575

## 576 **METHODS**

### 577 **Animals and tissue preparation**

578 All animal procedures adhered to the laws governing animal experimentation issued by the  
579 German Government. For all experiments, we used 5- to 18-week-old mice of either sex. For  
580 OPL recordings, we used Cx57<sup>+/+</sup> (n = 9; (Ströh et al., 2013)) mice, which were negative for  
581 Cre recombinase on both alleles and, therefore, could be considered wild-type animals. In  
582 addition, we used the HR2.1:TN-XL (n = 3) mouse line where the calcium indicator TN-XL  
583 was exclusively expressed in cones (Suppl. Fig. S8) (Wei et al., 2012). For IPL recordings,  
584 we used ChAT<sup>Cre</sup> (n = 5, JAX 006410, The Jackson Laboratory; (Rossi et al., 2011)) mice and  
585 for GCL recordings we used C57Bl/6 (n = 11, JAX 000664) or Pvalb<sup>Cre</sup> (n = 9, JAX 008069;  
586 ((Hippenmeyer et al., 2005)) mice. The transgenic lines ChAT<sup>Cre</sup> and Pvalb<sup>Cre</sup> were crossbred  
587 with the Cre-dependent red fluorescent reporter line Ai9<sup>tdTomato</sup> (JAX 007905). Owing to the  
588 exploratory nature of our study, we did not use randomization and blinding. No statistical  
589 methods were used to predetermine sample size.

590 Animals were housed under a standard 12 h day/night rhythm. For activity recordings,  
591 animals were dark-adapted for  $\geq 1$  h, then anaesthetized with isoflurane (Baxter) and killed by  
592 cervical dislocation. The eyes were enucleated and hemisected in carboxygenated (95% O<sub>2</sub>,  
593 5% CO<sub>2</sub>) artificial cerebrospinal fluid (ACSF) solution containing (in mM): 125 NaCl, 2.5 KCl,  
594 2 CaCl<sub>2</sub>, 1 MgCl<sub>2</sub>, 1.25 NaH<sub>2</sub>PO<sub>4</sub>, 26 NaHCO<sub>3</sub>, 20 glucose, and 0.5 L-glutamine (pH 7.4).  
595 Then, the tissue was either electroporated (see below) or moved to the recording chamber,  
596 where it was continuously perfused with carboxygenated ACSF at  $\sim 36$  °C. In all experiments,  
597 ACSF contained  $\sim 0.1$   $\mu$ M Sulforhodamine-101 (SR101, Invitrogen) to reveal blood vessels  
598 and any damaged cells in the red fluorescence channel (Euler et al., 2009). All procedures  
599 were carried out under very dim red ( $>650$  nm) light.

### 600 **Bulk electroporation**

601 For recordings in the ganglion cell layer (GCL), the fluorescent calcium indicator  
602 Oregon-Green BAPTA-1 (OGB-1) was bulk electroporated as described before (Briggman  
603 and Euler, 2011; Baden et al., 2016). In brief, the retina was dissected from the eyecup,  
604 flat-mounted onto an Anodisc (#13, 0.2  $\mu$ m pore size, GE Healthcare) with the GCL facing  
605 up, and placed between two 4-mm horizontal plate electrodes (CUY700P4E/L,  
606 Nepagene/Xceltis). A 10  $\mu$ l drop of 5 mM OGB-1 (hexapotassium salt; Life Technologies) in  
607 ACSF was suspended from the upper electrode and lowered onto the retina. After application  
608 of 9 pulses ( $\sim 9.2$  V, 100 ms pulse width, at 1 Hz) from a pulse generator/wide-band amplifier  
609 combination (TGP110 and WA301, Thurlby handar/Farnell), the tissue was moved to the  
610 recording chamber of the microscope and left to recover for  $\sim 30$  minutes before the  
611 recordings started.

### 612 **Virus injection**

613 The viral construct AAV2.7m8.hSyn.iGluSnFR was generated in the Dalkara lab as described  
614 previously (Dalkara et al., 2013; Khabou et al., 2016). The iGluSnFR plasmid construct was  
615 provided by J. Marvin and L. Looger (Janelia Research Campus, USA). A volume of 1  $\mu$ l of  
616 the viral construct was then injected into the vitreous humour of 3- to 8-week-old mice  
617 anaesthetized with 10% ketamine (Bela-Pharm GmbH & Co. KG) and 2% xylazine (Rompun,  
618 Bayer Vital GmbH) in 0.9% NaCl (Fresenius). For the injections, we used a micromanipulator  
619 (World Precision Instruments) and a Hamilton injection system (syringe: 7634-01, needles:

620 207434, point style 3, length 51 mm, Hamilton Messtechnik GmbH). Imaging experiments  
621 were performed 3–4 weeks after injection. As iGluSnFR expression tended to be weaker in  
622 the central retina, most OPL and IPL scan fields were acquired in the medial to peripheral  
623 ventral or dorsal retina.

## 624 **Two-photon imaging**

625 We used a MOM-type two-photon microscope (designed by W. Denk, MPI, Heidelberg;  
626 purchased from Sutter Instruments/Science Products). The design and procedures have  
627 been described previously (Euler et al., 2009). In brief, the system was equipped with a  
628 mode-locked Ti:Sapphire laser (MaiTai-HP DeepSee, Newport Spectra-Physics), two  
629 fluorescence detection channels for iGluSnFR/OGB-1 (HQ 510/84, AHF/Chroma) and  
630 SR101/tdTomato (HQ 630/60, AHF), and a water immersion objective (W Plan-Apochromat  
631 20× /1.0 DIC M27, Zeiss). The laser was tuned to 927 nm for imaging iGluSnFR, OGB-1 or  
632 SR101, and to 1,000 nm for imaging tdTomato. For image acquisition, we used custom-made  
633 software (ScanM by M. Müller and T.E.) running under IGOR Pro 6.3 for Windows  
634 (Wavemetrics), taking time-lapsed 64 × 64 pixel image scans (at 7.8125 Hz) for OGB-1  
635 imaging in the GCL and 128 × 128 pixel image scans (at 3.9 Hz) for glutamate imaging in the  
636 outer plexiform layer (OPL). For vertical glutamate imaging in the IPL, we recorded  
637 time-lapsed 64 × 56 pixel image scans (at 11.16 Hz) using an electrically tunable lens as  
638 described previously (Zhao et al., 2019). For high resolution images, 512 × 512 pixel images  
639 were acquired. The positions of the fields relative to the optic nerve were routinely recorded.

640 Two-photon imaging introduces a constant laser-induced baseline activity (see below and  
641 (Euler et al., 2009, 2019)). While we found that green-sensitive cones in the mouse were  
642 somewhat more affected by this “background illumination”, this slight bias did not change the  
643 conclusions of this study (Suppl. Fig. S9).

## 644 **Light stimulation**

645 For light stimulation, we used two different systems. The first system focused a DLP projector  
646 (‘lightcrafter’ (LCr), DPM-E4500UVBGMKII, EKB Technologies Ltd) with internal UV and  
647 green light-emitting diodes (LEDs) through the objective (TTO). To optimize spectral  
648 separation of mouse M- and S-opsins, LEDs were band-pass filtered (390/576 Dualband,  
649 F59-003, AHF/Chroma). The second system used an LCr with a lightguide port  
650 (DPM-FE4500MKIIF) to couple in external, band-pass filtered UV and green LEDs (green:  
651 576 BP 10, F37-576; UV: 387 BP 11, F39-389; both AHF/Chroma), focused through the  
652 condenser (TTC) of the microscope (for details, see (Franke et al., 2019)). For glutamate  
653 recordings in the IPL, we solely used the TTO stimulator, while for OPL and GCL recordings  
654 we used both TTO and TTC. LEDs were synchronized with the microscope’s scan retrace.  
655 Stimulator intensity (as photoisomerization rate,  $10^3 P^*$  per s per cone) was calibrated as  
656 described previously (Franke et al., 2019) to range from ~0.5 (black image) to ~20 for M- and  
657 S-opsins, respectively. In addition, a steady illumination component of  $\sim 10^4 P^*$  per s per cone  
658 was present during the recordings because of two-photon excitation of photopigments  
659 (discussed in (Euler et al., 2009, 2019; Baden et al., 2013)). The light stimulus was centered  
660 to the recording field before every experiment. For all experiments, the tissue was kept at a  
661 constant mean stimulator intensity level for at least 15 s after the laser scanning started and  
662 before light stimuli were presented.

663

664 Two types of light stimuli were used for glutamate imaging in the OPL:

- 665 (a) full-field (700  $\mu\text{m}$  in diameter) UV and green flashes,
- 666 (b) center (150  $\mu\text{m}$  in diameter) and surround (annulus; full-field flashes sparing the
- 667 central 150  $\mu\text{m}$ ) UV and green flashes.

668 Three types of stimuli were used for glutamate imaging in the IPL:

- 669 (c) local (100  $\mu\text{m}$  in diameter) chirp (for details, see (Franke et al., 2017));
- 670 (d) 2 Hz sine-wave modulation of center and surround for UV and green LED; and
- 671 (e) a UV and green center-surround flicker stimulus, with intensity of center and surround
- 672 determined independently by a balanced 180-s random sequence at 10 Hz.

673 Three types of stimuli were used for calcium imaging in the GCL:

- 674 (f) full-field (700  $\mu\text{m}$  in diameter) chirp stimulus (for details, see (Baden et al., 2016));
- 675 (g) 0.3  $\times$  1 mm bright bar moving at 1 mm  $\text{s}^{-1}$  in eight directions (Briggman and Euler,
- 676 2011); and
- 677 (h) a UV and green center-surround flicker stimulus (250  $\mu\text{m}$  in diameter for center), with
- 678 intensity of center and surround determined independently by a balanced 300-s
- 679 random sequence at 5 Hz.

680 For recording calcium responses in HR2.1:TN-XL mice, we used full-field white flashes (2 s,

681 50% duty cycle). Sizes of center stimuli were selected to completely fill the scan field area of

682 the recordings and, therefore, did not correspond to RF center sizes of retinal neurons.

## 683 **Pharmacology**

684 All drugs were bath applied for at least 10 min before recordings. The following drug

685 concentrations were used: 50  $\mu\text{M}$  6,7-dinitroquinoxaline-2,3-dione (NBQX), ACSF with twice

686 the normal concentration of KCl (5 mM). Drug solutions were carboxygenated and warmed to

687  $\sim 36$   $^{\circ}\text{C}$  before application.

## 688 **Single-cell electrophysiology**

689 GCL cells were targeted using an infrared LED and CCD camera for intracellular recordings.

690 Electrodes were pulled on a P-1000 micropipette puller (Sutter Instruments) with resistances

691 of  $\sim 7$ -15 M $\Omega$  and filled with solution consisting of (in mM): 120 K-gluconate, 5 NaCl, 10 KCl, 1

692 MgCl<sub>2</sub>, 1 EGTA, 10 HEPES, 2 Mg-ATP, and 0.5 Tris-GTP, adjusted to pH 7.2 using 1 M KOH.

693 Data were acquired using an Axopatch 200B amplifier in combination with a Digidata 1440

694 (both: Molecular Devices), digitized at 20 kHz and analyzed offline using Igor Pro

695 (Wavemetrics). For recordings, we targeted GCL cells located in the medial retina allowing to

696 investigate the effect of the two-photon laser on both UV and green responses.

## 697 **Single cell injection and morphology reconstruction**

698 OGB-1-labelled GCL cells were targeted with electrodes ( $\sim 5$ -15 M $\Omega$ ) subsequent to

699 two-photon recordings. Single cells in the GCL were dye-filled with SR101 (Invitrogen) using

700 the buzz function (100-ms pulse) of the MultiClamp 700B software (Molecular Devices).

701 Pipettes were carefully retracted as soon as the cell began to fill. Approximately 20 min were

702 allowed for the dye to diffuse throughout the cell before imaging started. After recording, an

703 image stack was acquired to document the cell's morphology, which was then traced

704 semi-automatically using the Simple Neurite Tracer plugin implemented in Fiji  
705 ([https://imagej.net/Simple\\_Neurite\\_Tracer](https://imagej.net/Simple_Neurite_Tracer)). In cases of any warping of the IPL, as described  
706 before (Baden et al., 2016), we used the original image stack to correct the traced cells using  
707 custom-written scripts in IGOR Pro.

## 708 **Data analysis**

709 Data analysis was performed using IGOR Pro. Upon publication, all data will be available at  
710 [www.retinal-functomics.org](http://www.retinal-functomics.org).

### 711 *Pre-processing*

712 For GCL recordings, ROIs were defined semi-automatically by custom software as described  
713 before (Baden et al., 2016). For glutamate imaging in OPL and IPL, ROIs were defined  
714 automatically by custom correlation-based algorithms in IGOR Pro. Here, ROI sizes were  
715 restricted to match the sizes of cone (3-7  $\mu\text{m}$  diameter) and BC axon terminals (1-4  $\mu\text{m}$   
716 diameter) in OPL and IPL scans, respectively. For OPL recordings, a specific correlation  
717 threshold for each scan field was manually selected to account for differences in staining and  
718 signal-to-noise-ratio. For IPL recordings, correlation thresholds were determined  
719 automatically and varied across the IPL due to differences in iGluSnFR labeling and laser  
720 intensity (for details, see (Zhao et al., 2019)). For every ROI located in the IPL, depth was  
721 determined using the shortest distance of ROI center to TdT-labeled ChAT bands and  
722 normalized such that 0 and 1 corresponded to On and Off ChAT band, respectively.

723 To relate each ROIs functional properties to its location on the retina, we registered the  
724 orientation of the retina for all IPL and GCL recordings and calculated the linear distance of  
725 each ROI to the optic nerve. For most OPL recordings, we did not register the retinal  
726 orientation. Here, we used the previously described gradient in opsin expression (Applebury  
727 et al., 2000; Baden et al., 2013) to separate dorsal (mean center SC > 0) and ventral (mean  
728 center SC < 0) scan fields.

729 The glutamate or calcium traces for each ROI were extracted (as  $\Delta F/F$ ) using custom  
730 analysis code based on the image analysis toolbox SARFIA for IGOR Pro (Dorostkar et al.,  
731 2010) and resampled at 500 Hz. A stimulus time marker embedded in the recorded data  
732 served to align the traces relative to the visual stimulus with 2 ms precision. For this, the  
733 timing for each ROI was corrected for sub-frame time-offsets related to the scanning.

734 First, we de-trended the traces by high-pass filtering above  $\sim 0.1$  Hz. For all stimuli except for  
735 the center-surround flicker, we then computed the median activity  $r(t)$  across stimulus  
736 repetitions (n=4-5 repetitions for chirps, n=3 repetitions for sine, n=25-30 repetitions for  
737 full-field and center-surround flashes, n=3 repetitions for moving bars).

### 738 *Center-surround stimulus and event kernels*

739 We mapped the stimulus kernels to the center-surround flicker by computing the  
740 glutamate/calcium event-triggered average ("event-triggered stimulus kernels"). To this end,  
741 we differentiated the response trace and estimated a response threshold as:

$$742 \quad \sigma = \frac{\text{median}(|r(t)|)}{0.6745} \quad (1)$$

743

744 We then computed the glutamate/calcium transient-triggered average stimulus, weighting  
745 each sample by the amplitude of the transient:

$$746 \quad \mathbf{F}(x,y, \tau) = \frac{1}{M} \sum_{i=1}^M \mathbf{c}(t_i) \mathbf{S}(x,t_i + \tau) \quad (2)$$

747 Here,  $\mathbf{S}(x,t_i + \tau)$  is the stimulus,  $\tau$  is the time lag and  $M$  is the number of glutamate/calcium  
748 events.

749 Similarly, for estimating the average glutamate/calcium event kernel upon full-field  
750 stimulation, we first identified time points of full-field activation in the stimulus trace and then  
751 computed the stimulus-triggered average glutamate/calcium event (“stimulus-triggered event  
752 kernels”).

### 753 *Response quality indices*

754 Kernel quality ( $Q_{i_{\text{Kernel}}}$ ) was measured by comparing area under the curve ( $F_{\text{Area}}$ ) of each  
755 response kernel with the respective baseline:

$$756 \quad Q_{i_{\text{Kernel}}} = 1 - \frac{|F_{\text{Area(Baseline)}}|}{|F_{\text{Area(Kernel)}}|} \quad (3)$$

757 Event quality ( $Q_{i_{\text{Event}}}$ ) was measured by comparing area under the curve ( $F_{\text{Area}}$ ) of each event  
758 with the respective baseline:

$$759 \quad Q_{i_{\text{Event}}} = 1 - \frac{|F_{\text{Area(Baseline)}}|}{|F_{\text{Area(Event)}}|} \quad (4)$$

760 To measure how well a cell responded to the other stimuli used (chirp, sine modulation,  
761 full-field and center-surround flashes, moving bars), we computed the signal-to-noise ratio

$$762 \quad Q_i = \frac{\text{Var}[(C)r]_t}{(\text{Var}[C]_t)r} \quad (5)$$

763 where  $C$  is the  $T$  by  $R$  response matrix (time samples by stimulus repetitions), while  $(\cdot)_x$  and  
764  $\text{Var}[\cdot]_x$  denote the mean and variance across the indicated dimension, respectively (Baden et  
765 al., 2016; Franke et al., 2017).

766 For further analysis of chromatic responses, we used

- 767 (a) ROIs in the OPL if they showed hyperpolarizing center or full-field responses and  
768  $Q_{i_{\text{full-field}}} > 0.25$  ( $n=2,132/2,945$ ) or  $Q_{i_{\text{center-surround}}} > 0.25$  ( $n=2,008/2,589$ ). For analysis of  
769 surround responses, only ROIs with an antagonistic response showing an increase in  
770 glutamate release with  $F_{\text{Area(Surround)}} > (|F_{\text{Area(Center)}}|/10)$  were considered ( $n=1,057/2,589$ ).
- 771 (b) ROIs in the IPL if  $Q_{i_{\text{Kernel}}} > 0.6$  for center UV or green stimulus kernel ( $n=3,188/3,604$ ).
- 772 (c) ROIs in the GCL if  $Q_{i_{\text{Kernel}}} > 0.6$  for center UV or green stimulus kernel  
773 ( $n=n=5,922/8,429$ ). For group assignment of GCL cells, we in addition only used ROIs  
774 with  $Q_{i_{\text{Chirp}}} > 0.4$  or  $Q_{i_{\text{Bars}}} > 0.6$  ( $n=4,519/8,429$ ). In addition, we excluded scan fields  
775 for which less than 50% of all cells passed the above mentioned quality thresholds  
776 ( $n=2$  scan fields).

### 777 *Spectral contrast*

778 For estimating the chromatic preference of recorded cells, we computed a spectral contrast  
779 (SC) using the area-under-the-curve ( $F_{\text{Area}}$ ) of the mean glutamate traces (OPL recordings; cf.

780 Fig. 1e,g) or the center-surround stimulus kernels (IPL and GCL recordings; *cf.* Figs. 3d, 5c).  
781 For stimulus kernels of IPL and GCL ROIs, we first estimated absolute  $F_{Area}$  of each of the  
782 four conditions (UV and green center and surround) and then set  $F_{Area}$  estimated from kernels  
783 anticorrelated to the center kernel to negative values (e.g. antagonistic surround will have  
784 negative  $F_{Area}$ ).

785 Previously, SC has been estimated as Michelson contrast based on dendritic calcium signals  
786 in mouse HCs (Chapot et al., 2017), ranging from -1 to 1 for the cell responding solely to UV  
787 and green, respectively. However, this requires UV and green responses to have the same  
788 response polarity (e.g. only decreases in calcium to full-field responses (Chapot et al.,  
789 2017)). As both center and surround responses of cells in OPL, IPL and GCL recordings can  
790 have different response polarities to UV and green, we here distinguished three cases to  
791 estimate SC.

792 If green and UV responses had the same response polarity (e.g. cone (1) in Fig. 1e), SC was  
793 estimated as Michelson contrast:

$$794 \quad SC = \frac{|F_{Area(Green)}| - |F_{Area(UV)}|}{|F_{Area(Green)}| + |F_{Area(UV)}|} \quad (6-a)$$

795 If the green response had an expected response polarity (e.g. increase in glutamate release  
796 upon surround stimulation in cones; cone (2) in Fig. 1f) and the UV response was  
797 antagonistic, SC was estimated as

$$798 \quad SC = 1 + \frac{|F_{Area(UV)}|}{|F_{Area(Green)}|} \quad (6-b)$$

799 Similarly, if the UV response had an expected response polarity and the green response was  
800 antagonistic, SC was estimated according to

$$801 \quad SC = -1 - \frac{|F_{Area(Green)}|}{|F_{Area(UV)}|} \quad (6-c)$$

802 For estimating the difference in SC between center and surround ( $SC_{Diff}$ ), we used:

$$803 \quad SC_{Diff} = SC_{Surround} - SC_{Center} \quad (7)$$

#### 804 *Density recovery profiles*

805 To estimate density recovery profiles (DRPs; (Rodieck, 1991)) of OPL ROI masks, we first  
806 calculated the distance of each ROI to each other ROI within the scan field, binned the  
807 distances (bin size=2  $\mu$ m) and normalized each bin count to the bin area. Next, we estimated  
808 the mean DRP per scan field by averaging the histograms of all ROIs within a field ( $n=56 \pm$   
809 30 ROIs per scan field). To obtain the mean DRPs of all ROI masks, we used  $n=52$  scan  
810 fields.

811 For relating DRPs of the ROIs to anatomy, we used a recent EM dataset of reconstructed  
812 cone and rod terminals to estimate anatomical DRPs as described above (*cf.* Suppl. Fig. S1;  
813  $n=163/2095$  cone/rod terminals; (Behrens et al., 2016)). For calculating a cone DRP with 3%  
814 rods (*cf.* Suppl. Fig. S1d), we first calculated the density of rod terminals and then randomly  
815 placed 3% of the expected number of rod terminals across the reconstructed area.

816

817

### 818 *Field entropy*

819 Field entropy ( $S_{Field}$ ) was used to estimate the variability of chromatic tuning within single IPL  
820 and GCL scan fields (Suppl. Fig. S4). First, SC values of all ROIs within one scan field were  
821 binned (bin size: 0.2) and then  $S_{Field}$  was defined as

$$822 \quad S_{Field} = -\sum_i p_i \log_2 p_i \quad (8)$$

823 where  $i$  is the number of SC bins and  $p_i$  corresponds to the number of ROIs in the  $i^{\text{th}}$  bin.  
824  $S_{Field} = 0$  if all ROIs of one recording field are in the same SC bin and therefore have the  
825 same spectral tuning.  $S_{Field}$  increases if ROIs are equally distributed across multiple bins. In  
826 general, high field-entropy indicates high chromatic tuning heterogeneity within a single field.  
827 As the number of ROIs per scan field was larger for IPL than GCL recordings, we likely  
828 underestimated the difference in  $S_{Field}$  between IPL than GCL recordings.

### 829 *Full-field opponency*

830 To measure whether UV and green full-field responses were color-opponent, we calculated  
831 the linear correlation coefficient ( $\rho$ ) between UV and green event kernels. For further analysis  
832 of opponent cells (*cf.* Figs. 3f, 4f), we only used ROIs with  $\rho < -0.3$  and  $Q_{i_{Event}} > 0.25$ .

### 833 *Sine data*

834 To estimate the chromatic preference of a cell based on its response to sinusoidal modulation  
835 (Suppl. Fig. S3), we first quantified the response phase for every stimulus condition (UV and  
836 green center and surround). For every ROI, we cross-correlated the mean glutamate trace of  
837 each condition with the stimulus trace and converted the time shift of maximal correlation into  
838 degrees. We then extracted the amplitude of the fundamental response component (F1) from  
839 the mean glutamate traces using Fourier transform. For the polar plot, response phases of  
840 different ROIs were binned using a bin size of  $15^\circ$  and each polar histogram was normalized  
841 according to its mean F1 amplitude. We performed this analysis for ventral and dorsal On  
842 (IPL depth  $< 0.2$ ) and Off (IPL depth  $> 0.5$ ) ROIs separately.

### 843 *Direction selectivity*

844 Direction selectivity (DS) of recorded GCL cell was computed as described before (Baden et  
845 al., 2016). In brief, we first performed singular value decomposition (SVD) on the mean  
846 response matrix (time samples by number of directions) of each cell. This decomposes the  
847 response into a temporal component and a direction dependent component or tuning curve.  
848 An advantage of this procedure is that it does not require manual selection of time bins for  
849 computing direction tuning but extracts the direction-tuning curve given the varying temporal  
850 dynamics of different neurons.

851 To measure DS, we computed the vector sum in the 2D plane and used the resulting vector  
852 length as DS index. We additionally assessed the statistical significance of direction tuning  
853 using a permutation test (Ecker et al., 2014). Here, we created surrogate trials by shuffling  
854 the trial labels, computing the tuning curve and vector sum for each surrogate trial. Carrying  
855 out this procedure 1,000 times generated a null distribution, assuming no direction tuning. We  
856 used the percentile of the true vector length as the P value for the direction tuning.

### 857 *Clustering of GCL cells*

858 The pre-processed ROI traces of GCL cells ( $n=4,519/8,429$ ) were assigned to previously  
859 identified functional RGC cluster (Baden et al., 2016) by identifying for each cell the cluster

860 with the best matching response properties. To account for a slight mismatch in frame rate for  
861 our stimulation systems compared to the previous one, calcium traces were shifted in time  
862 ( $t=40$  ms) and smoothed (for chirp stimulus only, boxcar smoothing with  $n=5$  points  
863 corresponding to 0.64 s) before calculating the linear correlation coefficients between a GCL  
864 cell's mean trace and all matching cluster mean traces for the chirp and the moving bar  
865 stimuli. Specifically, DS cells were correlated with DS clusters, non-DS cells were correlated  
866 with non-DS clusters, and alpha cells (soma area  $> 170 \mu\text{m}^2$ ) were correlated with alpha cell  
867 clusters. To combine stimulus-specific correlations and response quality, we generated an  
868 overall match index ( $Mi$ ) of each GCL cell to all RGC clusters (Román Rosón et al., 2019):

$$869 \quad Mi = \frac{Q_{i_{Chirp}}}{Q_{i_{Chirp}} + Q_{i_{Bar}}} * r_{Chirp} + \frac{Q_{i_{Bar}}}{Q_{i_{Chirp}} + Q_{i_{Bar}}} * r_{Ba}. \quad (9)$$

870 Finally, each GCL cell with  $Mi > 0.5$  was assigned to the cluster with the highest  $Mi$  and  
871 clusters were combined into functional RGC groups as described before (Baden et al., 2016).

## 872 *Statistical analysis*

873 We used the non-parametric Wilcoxon signed-rank test for quantifying the difference between  
874 cone surround responses under control and NBQX conditions (Fig. 2f), and field entropy of  
875 IPL and GCL scan fields (Suppl. Fig. S4).

876 We used the Chi-squared test to compare the distribution of anatomical and functional cone  
877 arrays (Suppl. Fig. S1h).

878 We used a Linear Mixed-Effects Model to analyze the difference between center and  
879 surround SC for OPL (Fig. 2b,c), IPL (Fig. 4b) and GCL recordings (Fig. 6b). This allowed to  
880 incorporate a random effects term in a linear predictor expression accounting for the fact that  
881 not all ROIs with a center response displayed a surround response (partially paired data). We  
882 used the `lme4`-package for R to implement the model and perform statistical testing (Bates et  
883 al., 2015). For details, see "Results of statistical analysis" in Suppl. Information.

884 We used Generalized Additive Models (GAMs) to analyze the relationship of difference in  
885 center and surround SC ( $SC_{Diff}$ ) and IPL depth (Fig. 4e); opponency and IPL depth (Fig. 4f);  
886 center chromatic preference ( $SC_{center}$ ) and IPL depth (Suppl. Fig. S2b). GAMs extend the  
887 generalized linear model by allowing the linear predictors to depend on arbitrary smooth  
888 functions of the underlying variables (Wood, 2006). In practise, we used the `mgcv`-package  
889 for R to implement GAMs and perform statistical testing. For details, see "Results of  
890 statistical analysis" in Suppl. Information.

891 To test if the number of color-opponent cells within single RGC and dAC groups was  
892 significantly larger/lower than expected from center SC and  $SC_{Diff}$ , we used a permutation test  
893 (Fig. 7g). First, we binned  $SC_{Diff}$  values across all groups (bin size=0.25). For every cell  
894 assigned to one group, we then randomly picked a different cell within the same  $SC_{Diff}$  bin  
895 and with a similar center SC ( $\pm 0.1$ ). Like this, we generated an "across-group" distribution of  
896  $SC_{Diff}$  values with similar mean and s.d., but with shuffled cell labels. Then, we estimated the  
897 percentage of color-opponent cells in this "across-group" distribution and repeated this  
898 procedure for 10,000 times per group, generating a null distribution. Finally, we used the  
899 percentile of the true percentage of color-opponent cells as the P value.

900

901 **REFERENCES**

- 902 Ahnelt PK, Schubert C, Kübber-Heiss A, Schiviz A, Anger E (2006) Independent variation of  
903 retinal S and M cone photoreceptor topographies: A survey of four families of mammals.  
904 *Vis Neurosci* 23:429–435.
- 905 Applebury ML, Antoch MP, Baxter LC, Chun LL, Falk JD, Farhangfar F, Kage K, Krzystolik  
906 MG, Lyass LA, Robbins JT (2000) The murine cone photoreceptor: a single cone type  
907 expresses both S and M opsins with retinal spatial patterning. *Neuron* 27:513–523.
- 908 Baden T, Berens P, Franke K, Román Rosón M, Bethge M, Euler T (2016) The functional  
909 diversity of retinal ganglion cells in the mouse. *Nature* 529:345–350.
- 910 Baden T, Osorio D (2019) The Retinal Basis of Vertebrate Color Vision. *Annu Rev Vis Sci*  
911 Available at: <http://dx.doi.org/10.1146/annurev-vision-091718-014926>.
- 912 Baden T, Schubert T, Chang L, Wei T, Zaichuk M, Wissinger B, Euler T (2013) A tale of two  
913 retinal domains: near-optimal sampling of achromatic contrasts in natural scenes  
914 through asymmetric photoreceptor distribution. *Neuron* 80:1206–1217.
- 915 Bae JA, Mu S, Kim JS, Turner NL, Tartavull I, Kemnitz N, Jordan CS, Norton AD, Silversmith  
916 WM, Prentki R, Sorek M, David C, Jones DL, Bland D, Sterling ALR, Park J, Briggman  
917 KL, Seung HS, Eyewirers (2018) Digital museum of retinal ganglion cells with dense  
918 anatomy and physiology. *Cell* 173:1293–1306.e19.
- 919 Barlow, BH (1961) Possible principles underlying the transformation of sensory messages.  
920 In: *Sensory Communication*. MIT Press.
- 921 Bates D, Mächler M, Bolker B, Walker S (2015) Fitting linear mixed-effects models using  
922 lme4. *Journal of Statistical Software* 67:1–48.
- 923 Behrens C, Schubert T, Haverkamp S, Euler T, Berens P (2016) Connectivity map of bipolar  
924 cells and photoreceptors in the mouse retina. *Elife* 5:e29941.
- 925 Breuninger T, Puller C, Haverkamp S, Euler T (2011) Chromatic bipolar cell pathways in the  
926 mouse retina. *J Neurosci* 31:6504–6517.
- 927 Briggman KL, Euler T (2011) Bulk electroporation and population calcium imaging in the adult  
928 mammalian retina. *J Neurophysiol* 105:2601–2609.
- 929 Burkhardt DA (1995) The influence of center-surround antagonism on light adaptation in  
930 cones in the retina of the turtle. *Vis Neurosci* 12:877–885.
- 931 Buzás P, Blessing EM, Szmajda BA, Martin PR (2006) Specificity of M and L cone inputs to  
932 receptive fields in the parvocellular pathway: random wiring with functional bias. *J*  
933 *Neurosci* 26:11148–11161.
- 934 Calderone JB, Jacobs GH (1995) Regional variations in the relative sensitivity to UV light in  
935 the mouse retina. *Vis Neurosci* 12:463–468.
- 936 Calderone JB, Reese BE, Jacobs GH (2003) Topography of photoreceptors and retinal  
937 ganglion cells in the spotted hyena (*Crocuta crocuta*). *Brain Behav Evol* 62:182–192.
- 938 Calkins DJ, Tsukamoto Y, Sterling P (1998) Microcircuitry and mosaic of a blue-yellow  
939 ganglion cell in the primate retina. *J Neurosci* 18:3373–3385.
- 940 Carter-Dawson LD, LaVail MM (1979) Rods and cones in the mouse retina. I. Structural  
941 analysis using light and electron microscopy. *J Comp Neurol* 188:245–262.
- 942 Chang L, Breuninger T, Euler T (2013) Chromatic coding from cone-type unselective circuits  
943 in the mouse retina. *Neuron* 77:559–571.
- 944 Chan TL, Grünert U (1998) Horizontal cell connections with short wavelength-sensitive cones

- 945 in the retina: a comparison between New World and Old World primates. *J Comp Neurol*  
946 393:196–209.
- 947 Chapot CA, Behrens C, Rogerson LE, Baden T, Pop S, Berens P, Euler T, Schubert T (2017)  
948 Local signals in mouse horizontal cell dendrites. *Curr Biol* 27:3603–3615.e5.
- 949 Chun M-H, Grünert U, Martin PR, Wässle H (1996) The synaptic complex of cones in the  
950 fovea and in the periphery of the macaque monkey retina. *Vision Res* 36:3383–3395.
- 951 Crook JD, Davenport CM, Peterson BB, Packer OS, Detwiler PB, Dacey DM (2009a) Parallel  
952 ON and OFF cone bipolar inputs establish spatially coextensive receptive field structure  
953 of blue-yellow ganglion cells in primate retina. *J Neurosci* 29:8372–8387.
- 954 Crook JD, Manookin MB, Packer OS, Dacey DM (2011) Horizontal cell feedback without  
955 cone type-selective inhibition mediates “red–green” color opponency in midget ganglion  
956 cells of the primate retina. *Journal of Neuroscience* 31:1762–1772.
- 957 Crook JD, Troy JB, Packer OS, Vrieslande JD, Dacey DM (2009b) Contribution of excitatory  
958 and inhibitory conductances to receptive field structure in midget and parasol ganglion  
959 cells of macaque monkey retina. *J Vis* 9:57a – 57.
- 960 Dacey DM (2000) Parallel pathways for spectral coding in primate retina. *Annu Rev Neurosci*  
961 23:743–775.
- 962 Dacey DM, Lee BB (1994) The “blue-on” opponent pathway in primate retina originates from  
963 a distinct bistratified ganglion cell type. *Nature* 367:731–735.
- 964 Dacey DM, Lee BB, Stafford DK, Pokorny J, Smith VC (1996) Horizontal cells of the primate  
965 retina: cone specificity without spectral opponency. *Science* 271:656–659.
- 966 Dalkara D, Byrne LC, Klimczak RR, Visel M, Yin L, Merigan WH, Flannery JG, Schaffer DV  
967 (2013) In vivo–directed evolution of a new adeno-associated virus for therapeutic outer  
968 retinal gene delivery from the vitreous. *Sci Transl Med* 5:189ra76–ra189ra76.
- 969 Denman DJ, Luviano JA, Ollerenshaw DR, Cross S, Williams D, Buice MA, Olsen SR, Reid  
970 RC (2018) Mouse color and wavelength-specific luminance contrast sensitivity are  
971 non-uniform across visual space. *Elife* 7:e31209.
- 972 DeVries SH, Qi X, Smith R, Makous W, Sterling P (2002) Electrical coupling between  
973 mammalian cones. *Curr Biol* 12:1900–1907.
- 974 Dominy NJ, Lucas PW (2001) Ecological importance of trichromatic vision to primates.  
975 *Nature* 410:363–366.
- 976 Dorostkar MM, Dreosti E, Odermatt B, Lagnado L (2010) Computational processing of optical  
977 measurements of neuronal and synaptic activity in networks. *J Neurosci Methods*  
978 188:141–150.
- 979 Ecker AS, Berens P, Cotton RJ, Subramaniam M, Denfield GH, Cadwell CR, Smirnakis SM,  
980 Bethge M, Tolias AS (2014) State dependence of noise correlations in macaque primary  
981 visual cortex. *Neuron* 82:235–248.
- 982 Euler T, Franke K, Baden T (2019) Studying a light sensor with light: Multiphoton imaging in  
983 the retina. preprints Available at: <https://www.preprints.org/manuscript/201903.0244>.
- 984 Euler T, Hausselt SE, Margolis DJ, Breuninger T, Castell X, Detwiler PB, Denk W (2009)  
985 Eyecup scope—optical recordings of light stimulus-evoked fluorescence signals in the  
986 retina. *Pflügers Archiv - European Journal of Physiology* 457:1393–1414.
- 987 Feigenspan A, Janssen-Bienhold U, Hormuzdi S, Monyer H, Degen J, Söhl G, Willecke K,  
988 Ammermüller J, Weiler R (2004) Expression of connexin36 in cone pedicles and

- 989 OFF-cone bipolar cells of the mouse retina. *J Neurosci* 24:3325–3334.
- 990 Field GD, Gauthier JL, Sher A, Greschner M, Machado TA, Jepson LH, Shlens J, Gunning  
991 DE, Mathieson K, Dabrowski W, Paninski L, Litke AM, Chichilnisky EJ (2010) Functional  
992 connectivity in the retina at the resolution of photoreceptors. *Nature* 467:673–677.
- 993 Franke K, Berens P, Schubert T, Bethge M, Euler T, Baden T (2017) Inhibition decorrelates  
994 visual feature representations in the inner retina. *Nature* 542:439–444.
- 995 Franke K, Chagas AM, Zhao Z, Zimmermann MJY, Qiu Y, Szatko K, Baden T, Euler T (2019)  
996 An arbitrary-spectrum spatial visual stimulator for vision research. bioRxiv:649566  
997 Available at: <https://www.biorxiv.org/content/10.1101/649566v1>.
- 998 Gerl EJ, Morris MR (2008) The causes and consequences of color vision. *Evolution:  
999 Education and Outreach* 1:476–486.
- 1000 Greene MJ, Kim JS, Seung HS, EyeWriters (2016) Analogous convergence of sustained and  
1001 transient inputs in parallel On and Off pathways for retinal motion computation. *Cell Rep*  
1002 14:1892–1900.
- 1003 Haverkamp S, Grünert U, Wässle H (2000) The cone pedicle, a complex synapse in the  
1004 retina. *Neuron* 27:85–95.
- 1005 Haverkamp S, Wässle H, Duebel J, Kuner T, Augustine GJ, Feng G, Euler T (2005) The  
1006 primordial, blue-cone color system of the mouse retina. *J Neurosci* 25:5438–5445.
- 1007 Helmstaedter M, Briggman KL, Turaga SC, Jain V, Seung HS, Denk W (2013) Connectomic  
1008 reconstruction of the inner plexiform layer in the mouse retina. *Nature* 500:168–174.
- 1009 Hippenmeyer S, Vrieseling E, Sigrist M, Portmann T, Laengle C, Ladle DR, Arber S (2005) A  
1010 developmental switch in the response of DRG neurons to ETS transcription factor  
1011 signaling. *PLoS Biol* 3:e159.
- 1012 Hornstein EP, Verweij J, Schnapf JL (2004) Electrical coupling between red and green cones  
1013 in primate retina. *Nat Neurosci* 7:745–750.
- 1014 Huang SC, Chiou TH, Marshall J, Reinhard J (2014) Spectral sensitivities and color signals in  
1015 a polymorphic damselfly. *PLoS One* 9:e87972.
- 1016 Jacobs GH, Neitz J, Deegan JF 2nd (1991) Retinal receptors in rodents maximally sensitive  
1017 to ultraviolet light. *Nature* 353:655–656.
- 1018 Jacobs GH, Williams GA, Fenwick JA (2004) Influence of cone pigment coexpression on  
1019 spectral sensitivity and color vision in the mouse. *Vision Res* 44:1615–1622.
- 1020 Joesch M, Meister M (2016) A neuronal circuit for colour vision based on rod-cone  
1021 opponency. *Nature* 532:236–239.
- 1022 Kelber A, Vorobyev M, Osorio D (2003) Animal colour vision--behavioural tests and  
1023 physiological concepts. *Biol Rev Camb Philos Soc* 78:81–118.
- 1024 Khabou H, Desrosiers M, Winckler C, Fouquet S, Auregan G, Bemelmans A-P, Sahel JA,  
1025 Dalkara D (2016) Insight into the mechanisms of enhanced retinal transduction by the  
1026 engineered AAV2 capsid variant -7m8. *Biotechnol Bioeng* 113:2712–2724.
- 1027 Kim JS, Greene MJ, Zlateski A, Lee K, Richardson M, Turaga SC, Purcaro M, Balkam M,  
1028 Robinson A, Behabadi BF, Campos M, Denk W, Seung HS, EyeWriters (2014)  
1029 Space-time wiring specificity supports direction selectivity in the retina. *Nature*  
1030 509:331–336.
- 1031 Lind O, Mitkus M, Olsson P, Kelber A (2013) Ultraviolet sensitivity and colour vision in raptor  
1032 foraging. *J Exp Biol* 216:1819–1826.

- 1033 Marshak DW, Mills SL (2014) Short-wavelength cone-opponent retinal ganglion cells in  
1034 mammals. *Vis Neurosci* 31:165–175.
- 1035 Martin PR, Lee BB, White AJ, Solomon SG, Rüttiger L (2001) Chromatic sensitivity of  
1036 ganglion cells in the peripheral primate retina. *Nature* 410:933–936.
- 1037 Marvin JS, Borghuis BG, Tian L, Cichon J, Harnett MT, Akerboom J, Gordus A, Renninger  
1038 SL, Chen TW, Bargmann CI, Orger MB, Schreier ER, Demb JB, Gan W-B, Hires SA,  
1039 Looger LL (2013) An optimized fluorescent probe for visualizing glutamate  
1040 neurotransmission. *Nat Methods* 10:162–170.
- 1041 Maximov VV (2000) Environmental factors which may have led to the appearance of colour  
1042 vision. *Philos Trans R Soc Lond B Biol Sci* 355:1239–1242.
- 1043 Mills SL, Tian LM, Hoshi H, Whitaker CM, Massey SC (2014) Three distinct blue-green color  
1044 pathways in a mammalian retina. *J Neurosci* 34:1760–1768.
- 1045 Murphy-Baum BL, Taylor WR (2015) The synaptic and morphological basis of orientation  
1046 selectivity in a polyaxonal amacrine cell of the rabbit retina. *J Neurosci* 35:13336–13350.
- 1047 Neitz J, Neitz M (2011) The genetics of normal and defective color vision. *Vision Res*  
1048 51:633–651.
- 1049 Olveczky BP, Baccus SA, Meister M (2003) Segregation of object and background motion in  
1050 the retina. *Nature* 423:401–408.
- 1051 Packer OS, Verweij J, Li PH, Schnapf JL, Dacey DM (2010) Blue-yellow opponency in  
1052 primate S cone photoreceptors. *J Neurosci* 30:568–572.
- 1053 Peichl L (2005) Diversity of mammalian photoreceptor properties: adaptations to habitat and  
1054 lifestyle? *Anat Rec A Discov Mol Cell Evol Biol* 287:1001–1012.
- 1055 Peichl L, González-Soriano J (1994) Morphological types of horizontal cell in rodent retinae:  
1056 a comparison of rat, mouse, gerbil, and guinea pig. *Vis Neurosci* 11:501–517.
- 1057 Peichl L, Künzle H, Vogel P (2000) Photoreceptor types and distributions in the retinae of  
1058 insectivores. *Vis Neurosci* 17:937–948.
- 1059 Peichl L, Sandmann D, Boycott BB (1998) Comparative Anatomy and Function of  
1060 Mammalian Horizontal Cells. In: *Development and organization of the retina: From  
1061 molecules to function* (Chalupa LM, Finlay BL, eds), pp 147–172. Boston, MA: Springer  
1062 US.
- 1063 Pfeiffer K, Homberg U (2007) Coding of azimuthal directions via time-compensated  
1064 combination of celestial compass cues. *Curr Biol* 17:960–965.
- 1065 Potier S, Mitkus M, Kelber A (2018) High resolution of colour vision, but low contrast  
1066 sensitivity in a diurnal raptor. *Proc R Soc B* 285:20181036.
- 1067 Puller C, Haverkamp S (2011) Bipolar cell pathways for color vision in non-primate  
1068 dichromats. *Vis Neurosci* 28:51–60.
- 1069 Rabl K, Cadetti L, Thoreson WB (2005) Kinetics of exocytosis is faster in cones than in rods.  
1070 *J Neurosci* 25:4633–4640.
- 1071 Rodieck RW (1991) The density recovery profile: a method for the analysis of points in the  
1072 plane applicable to retinal studies. *Vis Neurosci* 6:95–111.
- 1073 Röhlich P, van Veen T, Szél A (1994) Two different visual pigments in one retinal cone cell.  
1074 *Neuron* 13:1159–1166.
- 1075 Román Rosón M, Bauer Y, Kotkat AH, Berens P, Euler T, Busse L (2019) Mouse dLGN  
1076 receives functional input from a diverse population of retinal ganglion cells with limited

- 1077 convergence. *Neuron* 102:462–476.e8.
- 1078 Rossi J, Balthasar N, Olson D, Scott M, Berglund E, Lee CE, Choi MJ, Lauzon D, Lowell BB,  
1079 Elmquist JK (2011) Melanocortin-4 receptors expressed by cholinergic neurons regulate  
1080 energy balance and glucose homeostasis. *Cell Metab* 13:195–204.
- 1081 Schlamp CL, Montgomery AD, Mac Nair CE, Schuart C, Willmer DJ, Nickells RW (2013)  
1082 Evaluation of the percentage of ganglion cells in the ganglion cell layer of the rodent  
1083 retina. *Mol Vis* 19:1387–1396.
- 1084 Shekhar K, Lapan SW, Whitney IE, Tran NM, Macosko EZ, Kowalczyk M, Adiconis X, Levin  
1085 JZ, Nimesh J, Goldman M, McCarroll SA, Cepko CL, Regev A, Sanes JR (2016)  
1086 Comprehensive classification of retinal bipolar neurons by single-cell transcriptomics.  
1087 *Cell* 166:1308–1323.e30.
- 1088 Sher A, DeVries SH (2012) A non-canonical pathway for mammalian blue-green color vision.  
1089 *Nat Neurosci* 15:952–953.
- 1090 Stabio ME, Sabbah S, Quattrochi LE, Ilardi MC, Fogerson PM, Leyrer ML, Kim MT, Kim I,  
1091 Schiel M, Renna JM, Briggman KL, Berson DM (2018) The M5 cell: A color-opponent  
1092 intrinsically photosensitive retinal ganglion cell. *Neuron* 97:150–163.e4.
- 1093 Ströh S, Sonntag S, Janssen-Bienhold U, Schultz K, Cimiotti K, Weiler R, Willecke K, Dedek  
1094 K (2013) Cell-specific cre recombinase expression allows selective ablation of glutamate  
1095 receptors from mouse horizontal cells. *PLoS One* 8:e83076.
- 1096 Szél A, Röhlich P, Caffé AR, Juliusson B, Aguirre G v., Van Veen T (1992) Unique  
1097 topographic separation of two spectral classes of cones in the mouse retina. *J Comp*  
1098 *Neurol* 325:327–342.
- 1099 Szikra T, Trenholm S, Drinnenberg A, Jüttner J, Raics Z, Farrow K, Biel M, Awatramani G,  
1100 Clark DA, Sahel J-A, da Silveira RA, Roska B (2014) Rods in daylight act as relay cells  
1101 for cone-driven horizontal cell-mediated surround inhibition. *Nat Neurosci* 17:1728–1735.
- 1102 Thoreson WB, Dacey DM (2019) Diverse cell types, circuits, and mechanisms for color vision  
1103 in the vertebrate retina. *Physiol Rev* 99:1527–1573.
- 1104 Tikidji-Hamburyan A, Reinhard K, Storchi R, Dietter J, Seitter H, Davis KE, Idrees S, Mutter  
1105 M, Walmsley L, Bedford RA, Ueffing M, Ala-Laurila P, Brown TM, Lucas RJ, Münch TA  
1106 (2017) Rods progressively escape saturation to drive visual responses in daylight  
1107 conditions. *Nat Commun* 8:1813.
- 1108 Trümpner J, Dedek K, Schubert T, de Sevilla Müller LP, Seeliger M, Humphries P, Biel M,  
1109 Weiler R (2008) Rod and cone contributions to horizontal cell light responses in the  
1110 mouse retina. *J Neurosci* 28:6818–6825.
- 1111 Verweij J, Kamermans M, Spekrijse H (1996) Horizontal cells feed back to cones by shifting  
1112 the cone calcium-current activation range. *Vision Res* 36:3943–3953.
- 1113 Wässle H, Riemann HJ (1978) The mosaic of nerve cells in the mammalian retina. *Proc R*  
1114 *Soc Lond B Biol Sci* 200:441–461.
- 1115 Wei T, Schubert T, Paquet-Durand F, Tanimoto N, Chang L, Koeppen K, Ott T, Griesbeck O,  
1116 Seeliger MW, Euler T, Wissinger B (2012) Light-driven calcium signals in mouse cone  
1117 photoreceptors. *J Neurosci* 32:6981–6994.
- 1118 Welch JF (1953) Formation of urinating “posts” by house mice (*Mus*) held under restricted  
1119 conditions. *J Mammal* 34:502–503.
- 1120 Wood SN (2006) Generalized additive models: an introduction with R. Chapman and  
1121 Hall/CRC Texts in Statistical Science.

- 1122 Wool LE, Packer OS, Zaidi Q, Dacey DM (2019) Connectomic identification and  
1123 three-dimensional color tuning of S-OFF midget ganglion cells in the primate retina. *J*  
1124 *Neurosci* Available at: <http://dx.doi.org/10.1523/JNEUROSCI.0778-19.2019>.
- 1125 Yin L, Smith RG, Sterling P, Brainard DH (2009) Physiology and morphology of  
1126 color-opponent ganglion cells in a retina expressing a dual gradient of S and M opsins. *J*  
1127 *Neurosci* 29:2706–2724.
- 1128 Zhao Z, Klindt D, Chagas AM, Szatko KP, Rogerson LE, Protti D, Behrens C, Dalkara D,  
1129 Schubert T, Bethge M, Franke K, Berens P, Ecker AS, Euler T (2019) The temporal  
1130 structure of the inner retina at a single glance. bioRxiv:743047 Available at:  
1131 <https://www.biorxiv.org/content/10.1101/743047v1>.
- 1132

1133 **ACKNOWLEDGMENTS**

1134 We thank G. Eske for excellent technical support, S. Haverkamp and T. Baden for feedback  
1135 and discussions and J. Marvin and L. Looger for providing the viral vector  
1136 (pAAV.hSyn.iGluSnFR). This work was supported by the German Federal Ministry of  
1137 Education and Research (BMBF: FKZ: 01GQ1002 and 01GQ1601), the German Research  
1138 Foundation (DFG: BE5601/4; SFB1233, project number 276693517; EXC 2064, project  
1139 number 390727645; SCU 2243/3-1) and the Max Planck Society (MPG: M.FE.A.KYBE0004).

1140

1141 **AUTHOR CONTRIBUTIONS**

1142 K.F. designed the study with input from T.E.; D.D. produced the iGluSnFR virus; K.F.  
1143 performed viral injections; M.K. performed OPL recordings with help from K.F. and T.S.; K.F.  
1144 performed IPL recordings; K.S. performed GCL recordings with help from K.F.; Y.R.  
1145 performed electrical recordings; M.K., K.F. and K.S. performed pre-processing; K.F. analyzed  
1146 the data with input from T.E. and P.B.; K.F. prepared the figures with help from K.S. and M.K.;  
1147 M.K., K.F., K.S., P.B. and T.E. wrote the manuscript.

1148